

Production of Λ and Σ^0 hyperons in proton-proton collisions

The COSY-TOF Collaboration

M. Abdel-Bary³, S. Abdel-Samad³, K-Th. Brinkmann^{1,8}, H. Clement⁴, J. Dietrich¹, E. Doroshkevich⁴, S. Dshemuchadse¹, K. Ehrhardt⁴, A. Erhardt⁴, W. Eyrich², D. Filges³, A. Filippi⁷, H. Freiesleben¹, M. Fritsch², W. Gast³, J. Georgi², A. Gillitzer³, J. Gottwald¹, D. Hesselbarth³, H. Jäger³, B. Jakob¹, R. Jäkel¹, L. Karsch¹, K. Kilian³, H. Koch⁹, M. Krapp², J. Kreß⁴, E. Kuhlmann¹, A. Lehmann², S. Marcello⁷, S. Marwinski³, S. Mauro⁹, W. Meyer⁹, P. Michel⁵, K. Möller⁵, H.P. Morsch^{3,6}, H. Mörtel², L. Naumann⁵, N. Paul³, L. Pinna², C. Pizzolotto², Ch. Plettner¹, S. Reimann¹, M. Richter¹, J. Ritman³, E. Roderburg³, A. Schamlott⁵, P. Schönmeier¹, W. Schroeder^{2,3}, M. Schulte-Wissermann^{1,a}, T. Seifzick³, F. Stinzig², M. Steinke⁹, G.Y. Sun¹, A. Teufel², W. Ullrich¹, G.J. Wagner⁴, M. Wagner², R. Wenzel¹, A. Wilms⁹, P. Wintz³, S. Wirth², P. Wüstner³, and P. Zupranski⁶

¹ Institut für Kern- und Teilchenphysik, Technische Universität Dresden, D-01062 Dresden, Germany

² Physikalisches Institut, Universität Erlangen-Nürnberg, D-91058 Erlangen, Germany

³ Institut für Kernphysik, Forschungszentrum Jülich, D-52425 Jülich, Germany

⁴ Physikalisches Institut, Universität Tübingen, D-72076 Tübingen, Germany

⁵ Institut für Kern- und Hadronenphysik, Forschungszentrum Dresden-Rossendorf, D-01314 Dresden, Germany

⁶ Soltan Institute for Nuclear Studies, 05-400 Swierk/Otwock, Poland

⁷ INFN Torino, 10125 Torino, Italy

⁸ Helmholtz Institut für Strahlen- und Kernphysik, Rheinische Friedrich-Wilhelm-Universität Bonn, D-53115 Bonn, Germany

⁹ Institut für Experimentalphysik, Ruhr-Universität Bochum, D-44780 Bochum, Germany

Received: 9 April 2010 / Revised: 19 June 2010

Published online: 11 September 2010

© The Author(s) 2010. This article is published with open access at Springerlink.com

Communicated by P. Braun-Munzinger

Abstract. This paper reports results on simultaneous measurements of the reaction channels $pp \rightarrow pK^+\Lambda$ and $pp \rightarrow pK^+\Sigma^0$ at excess energies of 204, 239, and 284 MeV (Λ) and 127, 162, and 207 MeV (Σ^0). Total and differential cross-sections are given for both reactions. It is concluded from the measured total cross-sections that the high-energy limit of the cross-section ratio is almost reached at an excess energy of only about 200 MeV. From the differential distributions observed in the overall CMS as well as in the Jackson and helicity frames, a significant contribution of interfering nucleon resonances to the Λ production mechanism is concluded while resonant Σ^0 production seems to be of lesser importance and takes place only through specific partial waves of the entrance channel. The data also indicate that kaon exchange plays a minor role in the case of Λ but an important role for Σ^0 production. Thus the peculiar energy dependence of the Λ/Σ^0 cross-section ratio appears in a new light as its explanation requires more than mere differences between the $p\Lambda$ and the $p\Sigma^0$ final-state interaction. The data provide a benchmark for theoretical models already available or yet to come.

1 Introduction

The physics program carried out at the COoler SYnchrotron COSY (Forschungszentrum Jülich, Germany) focuses on the study of mesons and baryons in the confinement regime of QCD. Associated strangeness production plays a major role within this general field and has been studied by various experimental groups at COSY. In the case of proton-proton-induced Λ and Σ^0 hyperon production this effort has led to very well-measured excitation functions

starting at excess energies ($\epsilon = \sqrt{s} - (m_p + m_K + m_Y)$) only a few MeV above the thresholds and extending to $\epsilon \approx 200$ MeV in the case of Λ and $\epsilon \approx 120$ MeV in the case of Σ^0 production [1–7].

One surprising result of these investigations is that the excitation function of $pp \rightarrow pK^+\Sigma^0$ exhibits within uncertainty a pure phase-space behavior ($\sigma_{\Sigma^0} \propto \epsilon^2$) whereas the $pK^+\Lambda$ final state is produced with larger abundance towards the production threshold. This leads to a peculiar energy dependence of the production cross-section ratio $R_{\Lambda/\Sigma^0} = \sigma_{\Lambda}/\sigma_{\Sigma^0}$. A few MeV above the threshold a high value of $R_{\Lambda/\Sigma^0} = 28_{-9}^{+6}$ has been found [3,4]. With

^a e-mail: m.schulte-wissermann@physik.tu-dresden.de

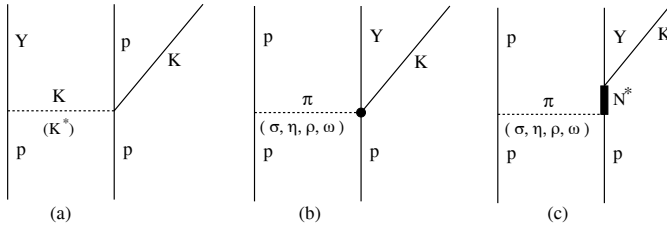


Fig. 1. Reaction mechanisms involving (a) strange, (b) non-resonant, and (c) resonant, non-strange meson exchange for $pp \rightarrow pK^+Y, Y = \Lambda, \Sigma^0$. Initial- and final-state interactions are not indicated.

increasing excess energy R_{Λ/Σ^0} drops steadily to a value of 8 ± 2.7 at $\epsilon = 60$ MeV [5]. Then, up to $\epsilon = 700$ MeV the energy dependence of R_{Λ/Σ^0} cannot be determined in a model-independent manner, as the few existing data points were taken at different excess energies. However, above 700 MeV the data collected in [8] show R_{Λ/Σ^0} to stay essentially constant at a value of only 2.2 ± 0.2 . The low- and the high-energy limits, respectively, are both close to “magic values”, as a ratio of 27 is the $SU(6)$ prediction of the ratio of the squares of the coupling constants of the virtual exchange kaon ($g_{N\Lambda K}^2/g_{N\Sigma K}^2$) [9] and the ratio of three follows from isospin considerations. It has been argued, however, that these theoretical explanations are oversimplifications [10,11]; perhaps one observes only a fortuitous coincidence.

The dramatic change of the Λ to Σ^0 cross-section ratio with excess energy could be due to different production processes, or distinctively different final-state interactions (FSI), or both. However, the reaction mechanisms are far from being established as various theoretical approaches have been developed in the last years which all reproduce the experimental data with about the same amount of success. These models are based on very different footings: a coherent interplay of FSI and nucleon resonances was concluded for Λ production [10]; the production via established nucleon resonances was studied [11]; a contribution of an $N(1535)$ -resonance without any proton-hyperon FSI was suggested [12]; destructive interferences between π and K exchange contributions were considered [13]; and a constituent quark-gluon model with the inclusion of nucleon resonances was proposed [14]. Finally, a model based on kaon and pion exchange developed for SATURNE [15, 16] data ($\epsilon > 1$ GeV) long before the COSY era also reproduces the energy dependence of R_{Λ/Σ^0} fairly well, as without any adjustment of the parameters the ratio is only underestimated by 50% directly at threshold [17, 18]. Hence, the energy dependence of the total cross-sections alone is not at all sufficient to discriminate between these different theoretical approaches. Differential observables for both reaction channels are highly desired in order to set benchmarks for theoretical models.

This large variety of theoretical approaches to describe hyperon ($= Y$) production in proton-proton collisions can be ordered into two classes of production scenarios depicted in fig. 1. On the one hand, kaon (and K^*) exchange manifests strangeness in the production mecha-

nism itself. In this case resonances could be involved in principle, however, none is known in the Kp -system at present. On the other hand, π (and $\sigma, \eta, \rho, \omega$) exchange shifts the strangeness production away from the interaction of both protons to the $p\pi \rightarrow KY$ vertex. Since the subprocess $p\pi \rightarrow KY$ is likely to involve an intermediate resonance ($p\pi \rightarrow N^*, \Delta^*; N^*/\Delta^* \rightarrow KY$), this scenario suggests the role of resonances to be of importance for proton-proton-induced hyperon production.

Numerous studies of nucleon and Δ -resonances excited in πN and γN reactions revealed among other resonances those which decay into particles with open strangeness such as the associated pairs $K\Lambda$ or $K\Sigma$ [19–24]. According to these findings and other experimental as well as theoretical work, the Particle Data Group [25] lists the resonances $N(1650)S_{11}$, $N(1675)D_{15}$, $N(1680)F_{15}$, $N(1700)D_{13}$, $N(1710)P_{11}$, $N(1720)P_{13}$, and $N(1900)P_{13}$ and values for the $K^+\Lambda$ branching ratios. Strong evidence was advanced for additional states, namely $N(1840)P_{11}$ and $N(1875)D_{13}$ [26]. The latter may be the same as $N(1895)D_{13}$ [27, 28] or $N(1950)D_{13}$ [29]. The properties of all these resonances (mass, width, branching ratios to $K\Lambda$ or $K\Sigma$) are typically not known well and the role these nucleon resonances play for associated strangeness production in proton-proton collisions is not well understood. It should be mentioned that the concept of resonant hyperon production limits the $K^+\Lambda$ final state to be produced only from N^* -resonances (due to isospin conservation) whereas the $K^+\Sigma^0$ pair can be reached via both N^* and Δ^* resonances. In the latter case, $\Delta(1600)P_{33}$, $\Delta(1620)S_{31}$, $\Delta(1700)P_{33}$, $\Delta(1750)P_{33}$, and $\Delta(1900)S_{31}$ can also be involved. The Δ^* -resonances increases the number of possible contributions to the $K^+\Sigma^0$ production process and renders a theoretical description even more difficult than that of the $pK^+\Lambda$ channel. Turning the argument around the isospin-selective $pp \rightarrow pK^+\Lambda$ channel could potentially serve as a tool to find so-called missing resonances (with $I = 1/2$) [30], *i.e.* resonant states predicted by quark models which have not been found experimentally so far.

The COSY-TOF Collaboration has recently published data on total cross-sections for the $pp \rightarrow pK^+\Lambda$ channel at moderate excess energies of 85, 115, and 171 MeV, and the first differential data, namely Dalitz plots and helicity angle distributions at $\epsilon = 171$ MeV [6]. In addition, invariant-mass spectra are shown. The results can be described by a reaction model which includes in a coherent manner the $N(1650)S_{11}$, $N(1710)P_{11}$, and $N(1720)P_{13}$ nucleon resonances in conjunction with a considerable contribution of $p\Lambda$ final-state interaction. With increasing energy the relative contribution of the $N(1650)S_{11}$ then diminishes in trade for a stronger influence of the $N(1710)P_{11}$ and $N(1720)P_{13}$ as shown in [31, 32].

The only known experimental fact in the case of the $pp \rightarrow pK^+\Sigma^0$ reaction is the proportionality of the total cross-section to the phase-space volume ($\sigma_{\Sigma^0} \propto \epsilon^2$). This can be taken as an indication for the reaction mechanism to be independent of the excess energy and the absence of a strong $p\Sigma^0$ -FSI which would manifest itself close to threshold. However, it is of course possible that competing

processes cancel in a way that they mimic the $\sigma_{\Sigma^0} \propto \epsilon^2$ behavior. As experimental results on differential observables are completely lacking for Σ^0 production in pp -collisions any detailed theoretical approach is currently hampered strongly.

In this paper differential distributions for both reactions are presented, namely the angular distributions of all final-state particles in the overall CMS, as well as distributions in both the Jackson and helicity frames of all two-body subsystems. Like Dalitz plots, the helicity angle distributions provide insight into the three-body final state. They are especially well suited to investigate the influence of intermediate resonances. The information contained in the Jackson angle distributions is complementary to that of a Dalitz plot, as this angular distribution relates the exit to the entrance channel and hints at relative angular momenta and/or resonances present in a specific two-body subsystem.

The data were taken at beam momenta of $p_{beam} = 2950, 3059$, and $3200 \text{ MeV}/c$. These beam momenta correspond to excess energies of 204, 239, and 284 MeV in the case of $pp \rightarrow pK^+\Lambda$ ($m_\Lambda = 1116 \text{ MeV}$) while the neutral Σ is produced 127, 162, and 207 MeV above threshold ($m_{\Sigma^0} = 1193 \text{ MeV}$). The data taken at $p_{beam} = 3059 \text{ MeV}/c$ stand out since they have a large integrated luminosity; in this case the calibration, the acceptance¹ correction as well as the overall luminosity were cross-checked by three independent subgroups of our collaboration when a supposed pentaquark state was searched for [33]. The measurements at $2950 \text{ MeV}/c$ and $3200 \text{ MeV}/c$ were carried out directly one after the other without any change of detector set-up, DAQ, high voltage or electronics. Hence, the results of these two data sets are ideal for relative comparisons as systematic uncertainties partly cancel.

2 Experimental procedure

2.1 Detector setup

The experiments were carried out with the time-of-flight detector COSY-TOF located at an external beam line of the COoler SYnchrotron COSY (Forschungszentrum Jülich). The COSY machine provides proton beams of very high quality (spill length $\approx 5 \text{ min}$; several 10^6 protons/s; low emittance of $< 5 \pi \text{ mm mrad}$; relative momentum uncertainty $\Delta p/p < 10^{-3}$).

The layout of the COSY-TOF detector is shown in the upper part of fig. 2; in the lower part the near target region with the time-of-flight start and tracking detectors [34,35] is sketched. The interaction volume is small and well defined as the narrow beam with Gaussian profile ($\sigma_{x,y} < 300 \mu\text{m}$) is directed onto a liquid-hydrogen target of only 4 mm length [36]. The emerging particles traverse just behind the target ($\approx 25 \text{ mm}$) a 24-fold segmented scintillation detector ("start-detector") which provides the start signal for the time-of-flight measurement.

¹ The term "acceptance" is used for the convolution of solid-angle coverage, detector, and reconstruction efficiency.

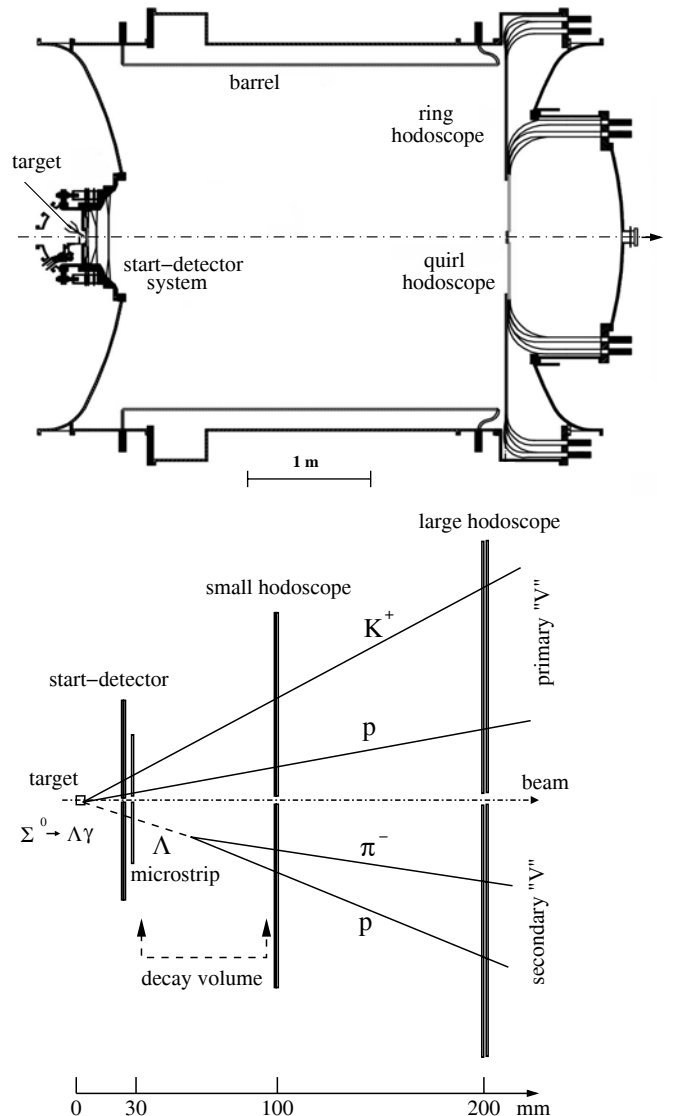


Fig. 2. The COSY-TOF detector (top), the near-target region (start-detector system, bottom). Within the lower picture the event pattern for both hyperon channels is shown.

At a distance of 30 mm downstream of the target a double-sided silicon-microstrip detector is installed, followed by two double-layered scintillating fiber hodoscopes at 100 and 200 mm. These three tracking detectors measure the coordinates of traversing charged particles in three dimensions with a spatial resolution of $\approx 100 \mu\text{m}$ (microstrip) and $\approx 1.5 \text{ mm}$ (hodoscopes).

After a flight path of $\approx 3 \text{ m}$ through the evacuated vessel (0.2 Pa) all charged particles are detected in the highly segmented stop components. They consist of two triple-layered forward hodoscopes (central and ring hodoscope) [37] and a barrel hodoscope [38], all manufactured from BC412 scintillating material. From the combined measurement of time and position the velocity vectors of all charged particles are determined with a time-of-flight resolution of better than $\sigma_{TOF} = 300 \text{ ps}$ and an angular track resolution of better than $\sigma_\Delta = 0.3^\circ$.

Primary vertices (located within the target) are reconstructed with an accuracy of better than $\sigma_{x,y} = 0.5$ mm and $\sigma_z = 2.0$ mm. Secondary vertices from particles decaying behind the microstrip detector and before the first hodoscope are reconstructed with an accuracy of $\sigma_{x,y} < 1$ mm and $\sigma_z < 3.0$ mm.

The COSY-TOF detector stands out for its low-mass area density of target, start-detector, and tracking detectors. This renders the influence of small-angle scattering and energy loss almost negligible. In addition, the COSY-TOF detector has a high efficiency of $> 95\%$ for the detection of charged particles and covers a large solid angle ($1^\circ < \theta < 60^\circ$, $0^\circ < \phi < 360^\circ$) in the laboratory frame. These features allow the almost unambiguous and simultaneous identification of different reaction channels (*e.g.*, $pp \rightarrow pp$, $d\pi^+$, $pp\omega$, $pK^+\Lambda$, $pK^+\Sigma^0$, $pK^0\Sigma^+$) by examining the measured time of flight of the charged particles and their event topology.

2.2 Principle of measurement and data analysis

The strategies presented in this paper for the analysis of neutral hyperon production are a straightforward extension of the special routines developed by the Dresden group for the analysis of the reaction channel $pp \rightarrow pK^0\Sigma^+$ (analysis A in [33]) within our standard analysis framework [39–42]. This approach is an alternative one to that applied in [6,35].

Here, the focus lies on an extensive use of the time-of-flight information in order to independently determine, on the one hand, the primary particles (p, K^+) and, on the other hand, the secondary particles stemming from the hyperon's decay into p and π^- . While the secondary particles are used as a “positive tag” for a pK^+Y events, the four-momenta of primary protons and kaons are utilized to calculate the missing-mass spectrum which shows both hyperons well resolved. This missing-mass spectrum is then the backbone of the analysis.

The simultaneous analysis of the reactions $pp \rightarrow pK^+\Lambda$ and $pp \rightarrow pK^+\Sigma^0$ is possible due to the decay properties of the hyperons involved. A Σ^0 ($m_{\Sigma^0} = 1193$ MeV/ c^2) decays with a branching ratio of $\mathcal{BR} \approx 100\%$ in the direct vicinity of its production vertex ($c\tau = 2.2 \cdot 10^{-11}$ m) to $\Lambda\gamma$. The photon remains undetected, however, its energy is small compared to the mass of the Λ ($m_\Lambda = 1116$ MeV/ c^2) and thus the change of direction of the Λ with respect to that of the Σ^0 is less than 5° in the laboratory system. This minor change of direction justifies to analyze both reactions on equal footing.

During data taking both final states are preselected via the same trigger based on the multiplicity jump of charged particles (see fig. 2, lower part): near the target (start-detector) only two charged particles are found (p, K^+) whereas, due to the sizable decay length of the Λ hyperon ($c\tau_\Lambda = 7.89$ cm) and its decay into two charged particles ($\Lambda \rightarrow p\pi^-$, $\mathcal{BR} = 64.2\%$), four hits are detected in the stop components. This requirement is also modeled as the first step in the off-line analysis.

Both primary (p, K^+) and secondary (p, π^-) particles emerge from a vertex and form a V -shaped pattern in the detector. These patterns are searched for by a fitting procedure, where each layer of the tracking detectors, which has produced a signal, provides an individual track point. In order to identify these two different sets of V -shaped patterns the following self-evident conditions are exploited: a primary V is characterized by two hits in the stop components in coincidence with two hits in the start-detector together with any number of track points in the microstrip and hodoscopes; the vertex must be located inside the target within resolution. A secondary V has two hits in the stop components; at least three track points in each arm; a decay plane intersecting the target volume; and a decay vertex located in the volume between the microstrip detector and the first hodoscope (decay volume). All permutations of hits in the stop components are taken into account resulting first in a set of primary and then in secondary V -candidates. The best V 's are chosen according to the number of track points and the quality of the fit. This method was developed by means of Monte Carlo data.

So far only geometric information has been exploited in order to independently determine one primary and one secondary V . Using the measured time of flight ($t_{stop} - t_{start}$) for the particles of each arm of the primary V 's leads to corresponding primary velocity vectors. An averaged start-detector value is used for the time-of-flight determination of secondary particles. Masses have to be assigned to these velocity vectors in order to obtain four-vectors. As the COSY-TOF detector does not provide direct particle identification, the event topology is used. For the secondary V , the particle with the smaller angle to the direction of flight of the hyperon (determined from the primary to the decay vertex) is called “proton” while the other is called “pion”. Monte Carlo studies have shown that, due to the large mass difference of both particles, this assignment is correct for more than 99% of the $pK^+\Lambda$ events (97% in case of $pK^+\Sigma^0$).

In order to label each arm of the primary V correctly as proton and kaon the direction of flight of the hyperon is used. This observable is measured independently twice, 1) from the vector connecting the origin with the vertex of the secondary V and 2) from the missing momentum vector calculated from the primary particles. The latter is calculated for both possibilities of particle assignment, the one with the better match of flight directions is chosen to be the proper one. Monte Carlo studies have shown that the mass assignment is correct for about 80% of the events. Swapped mass assignments lead to a broad missing-mass distribution in the final data sample with no peaks in the vicinity of the hyperon masses.

The background is reduced by requiring the properties of the secondary V to match those of a decaying Λ hyperon. Firstly, it is necessary that the angle of the secondary proton with respect to the Λ flight direction lies within the kinematically possible region ($< 10^\circ$). Secondly, the invariant mass of proton and pion, $m_{p\pi^-} = m_\Lambda$, is calculated from the flight direction of the hyperon (decay vertex), the measured four-momentum of the

secondary proton, and the direction vector of the pion. This value must match the Λ mass within limits determined by Monte Carlo. The combination of both requirements reduces Monte Carlo and data signals by only 4% while 40% of the experimental background is suppressed in the final data sample.

As a final selection criterion, only events with the combined momentum vector of primary proton and kaon pointing in the backward CMS hemisphere are considered. Due to the Lorentz boost the particles in this hemisphere have smaller velocities in the laboratory system. This increases the relative time-of-flight resolution, which in turn significantly increases the absolute momentum, and hence, the missing-mass resolution. It should be mentioned that this requirement leads to no loss of physical information, as the symmetric entrance channel (proton-proton) enforces the same physics in either CMS hemisphere.

2.3 Acceptance correction and absolute normalization

The Monte Carlo package used [43, 44] models the detector and the physical processes to great detail. The event generator produces the particles of the exit channel either according to the three-body phase space, or likewise, intermediate resonances can be chosen in order to model a two-step creation process ($pp \rightarrow pN^*, N^* \rightarrow K^+\Lambda, K^+\Sigma^0$). The particles (and their daughters, grand-daughters, ...) are then propagated through the detector. Branching ratios and lifetimes of all particles are incorporated according to the values given in [25]. Energy loss, small-angle scattering, nuclear reactions, and δ -electrons are considered. From the energy deposit in the active detector components digitized QDC and TDC signals are generated. Noise and thresholds are modeled as known from the measured detector response. Deviations from an homogeneously populated phase space can be introduced by a weight function on an event-by-event basis (this procedure is called *filtering* in the following). Finally, the Monte Carlo data are subjected to the very same routines as real data in order to determine the acceptance.

The use of phase-space-distributed data as Monte Carlo input is only justified if the reaction under study is homogeneously distributed in phase space or if the acceptance coverage of the detector is homogeneous over the whole five-dimensional event space of the three-body final state. Two deviations from three-body phase space are likely to occur in proton-proton experiments: anisotropic angular distributions causing particles to prefer different angular regions (of possibly different acceptance) and intermediate nucleon resonances limiting the available phase space of all decay products caused by the mass and width of the resonance.

The influence of anisotropic angular distributions on the overall acceptance was investigated by filtering the Monte Carlo input in such a way as to match the experimental results. For all modeled angular distributions a change of the overall acceptance of less than 10% was found. The influence of nucleon resonances on the acceptance-corrected data was deduced by using a set of Monte Carlo data created with different N^* -resonances

($m_{N^*} = 1400, 1535, 1650, 1720, 1850, 1900$ MeV; $\Gamma_{N^*} = 20, 100, 150, 200, 300, 400$ MeV). Only minor changes of the acceptance-corrected differential distributions were observed and the total cross-section changes by less than 4% if the width of the resonance was chosen to be larger than 100 MeV. As, at present, there is no theoretical model available on which a proper Monte Carlo simulation can be based, a homogeneously populated phase space modified to model measured angular distributions was used throughout the analysis. Details will be given when discussing the angular distributions.

The overall acceptance for the reactions under study is mainly governed by three obvious contributions, namely the Λ branching ratio to charged particles (64%), the restriction to one CMS hemisphere (50%), and the probability of the secondary vertex to be located within the “decay volume” (30%) indicated in the lower part of fig. 2. The decay of kaons and pions in flight as well as a decay pion escaping detection contribute in an intertwined manner ($\approx 25\%$). The overall acceptance is found to be $\approx 1.8\%$ in case of Λ and $\approx 1.4\%$ in case of Σ^0 detection. The relative uncertainty of the acceptance correction was determined by investigating the effect of all restrictions imposed during the data analysis and was found to be below 10%.

In the case of differential distributions the acceptance varies smoothly with the observable under consideration. Here, an additional uncertainty comes into play due to the gradient of the acceptance function. This additional uncertainty Δa_i is taken into account by choosing $\Delta a_i = (|a_i - a_{i-1}| + |a_i - a_{i+1}|)/4$, where a_i is the acceptance in bin i . The square root of the quadratic sum of this acceptance uncertainty, the statistical error, and the uncertainty due to signal-background separation (see below) will be shown when presenting the data.

The absolute normalization is determined via the analysis of elastic scattering, which was recorded simultaneously during the experiment. Our results are normalized to high-quality data on elastic cross-sections provided by the EDDA Collaboration [45] and yielded the numerical values for the time-integrated luminosity of 16.9 nb^{-1} (2950 MeV/c), 214 nb^{-1} (3059 MeV/c), and 6.4 nb^{-1} (3200 MeV/c). The total uncertainty of this procedure (5%) is in equal parts due to our analysis and the uncertainty of the literature data. For details see [39, 40].

2.4 Determination of the signal yields

Figure 3 shows the missing-mass spectra measured at the three excess energies. In addition the Monte Carlo result is shown for a beam momentum of 3059 MeV/c (lower-right) The ratio of Monte Carlo $pK^+\Lambda$ and $pK^+\Sigma^0$ events are chosen according to the total cross-sections measured for each excess energy. Distinct signals for the Λ and the Σ^0 hyperon can be seen above a smooth and structureless background. As usual for time-of-flight detectors, the missing-mass resolution (momentum resolution) is best for smaller velocities in the exit channel (smaller beam momenta in the entrance channel). Comparing the spectra, the higher luminosity is reflected in the spectrum for

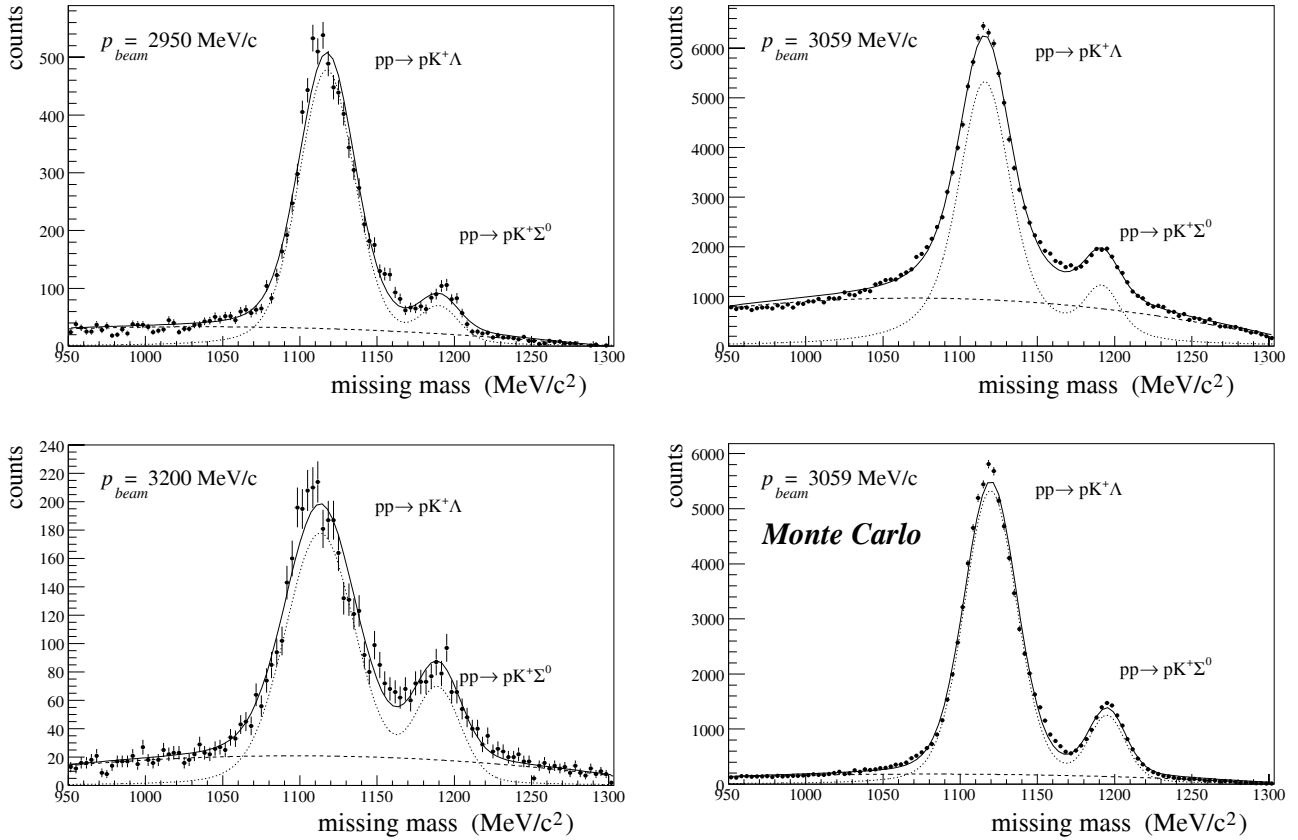


Fig. 3. Missing-mass spectra measured at the three beam momenta. Two peaks, corresponding to $pp \rightarrow pK^+\Lambda$ and $pp \rightarrow pK^+\Sigma^0$ are observed above a smooth background. The results of a fitting procedure for signal (dotted line), background (dashed line), and total spectrum (solid line) are shown in all cases. In the lower right frame the Monte Carlo result for 3059 MeV/c is depicted. The relative weight of both signals were accounted for by using the experimentally determined ratio of the total cross-sections.

$p_{beam} = 3059$ MeV/c, a better beam quality for the measurements at $p_{beam} = 2950$ and 3200 MeV/c manifests itself in a low background contribution.

The number of events in the missing-mass peaks are obtained by consecutively fitting first the background and then the signals. For the background parametrization quadratic or cubic polynomials are used, where only missing masses below the Λ and above the Σ^0 peak are taken into account. Both types of parametrizations lead to the same final results within 2%. Then, the background parameters are fixed and the signals are described by two Voigt functions (convolution of a Gauss and a Lorentz function). Voigt functions are chosen since they model properly the signal shape of a rather narrow peak accompanied by broader tails. A superposition of two Gaussians, however, yields the same results within uncertainty limits [46].

The overall systematic uncertainty due to signal and background separation is determined by varying the fit region for the background fit below and above the two peaks. In the case of Λ production this uncertainty is rather small (5%), especially as the contribution of the much smaller Σ^0 signal is negligible. The relative influence of the background on the systematic uncertainty is larger for the smaller Σ^0 signal (15%). Here, the signal-to-background ratio is close to unity and more sensitive to the choice of fitting regions. In addition, the uncertainty

of the contribution of the much larger Λ signal is not negligible, especially as the Σ^0 signal happens to appear near the maximum change of the slope of the Λ tail.

For the total cross-sections statistical uncertainties which reflect the numerical uncertainties of the fitting procedure are quoted while the systematic uncertainties are the quadratic sum of the uncertainties of luminosity determination (5%), acceptance correction (10%), and signal integration (5% for Λ and 15% for Σ^0).

Differential cross-sections are determined in analogy to the total yield, only that the amount of signal and background is determined individually from missing-mass spectra generated for each bin of the observable under study. The widths of the bins are chosen according to the detector resolution and statistical aspects. In addition, the secondary V is required to have in each arm four track points in the two hodoscopes. This requirement further reduces background and allows to separate a clean signal also in angular bins containing only a small number of counts.

3 Results and discussions

The interpretation of experimental data on proton-proton-induced hyperon production is difficult for three

Table 1. Total cross-sections for the reactions $pp \rightarrow pK^+\Lambda$ and $pp \rightarrow pK^+\Sigma^0$. The first uncertainty refers to statistical and the second to systematical ones.

ϵ (MeV)	acc (%)	counts	σ_{tot} (μb)
$pp \rightarrow pK^+\Lambda$			
204	1.95	7228	$21.8 \pm 0.3 \pm 2.7$
239	1.72	89684	$24.4 \pm 0.1 \pm 3.0$
284	1.63	3322	$32.0 \pm 0.9 \pm 3.9$
$pp \rightarrow pK^+\Sigma^0$			
127	1.28	676	$3.1 \pm 0.2 \pm 0.6$
162	1.51	12644	$3.9 \pm 0.1 \pm 0.7$
207	1.45	800	$8.6 \pm 0.5 \pm 1.6$

reasons. First off, the different reaction mechanisms (light/heavy non-strange as well as strange meson exchange, nucleon resonances, and FSI, ...) are likely to interfere, *i.e.* the effects of the different contributions cannot be seen in a pure and isolated manner. Second, each particle in a three-body final state is always connected kinematically to the other two. This can lead to correlations between two different observables and renders a true physical cause difficult to disentangle from its effect. A well-known example for this to happen is the reflection of a resonance seen in a Dalitz plot. And finally, the interpretation of the experimental data by theory is often ambiguous as different conclusions can be drawn from the same experimental data set. For these reasons the interpretation of the results presented will be using only general arguments based on kinematics and conservation laws.

In the following the total cross-sections for both channels will be presented and discussed, where in particular the energy dependence of the ratio R_{Λ/Σ^0} will be addressed. Then the differential distributions of the reaction $pp \rightarrow pK^+\Lambda$ will be shown for all three excess energies in various reference frames. Using these results we will elaborate on the reaction mechanism as it manifests itself in these differential distributions. Finally, the first differential observables for Σ^0 production in proton-proton collisions will be presented for the high statistics data set. Here the discussion will concentrate on a comparison of the two reaction channels and the reaction mechanisms involved. The numerical values of all differential cross-sections are listed in the appendix.

3.1 Total cross-sections

The results for the total cross-sections are listed in table 1. They are included in fig. 4 which shows in the upper part the world data of total cross-sections for the reaction $pp \rightarrow pK^+\Lambda$ and $pp \rightarrow pK^+\Sigma^0$ ($\epsilon < 300$ MeV). Our new data extend the near-threshold measurements by roughly 80 MeV excess energy, *i.e.* directly into the region where the energy dependence of the ratio of the cross-sections R_{Λ/Σ^0} is not known well. Up to $\epsilon \approx 170$ MeV the

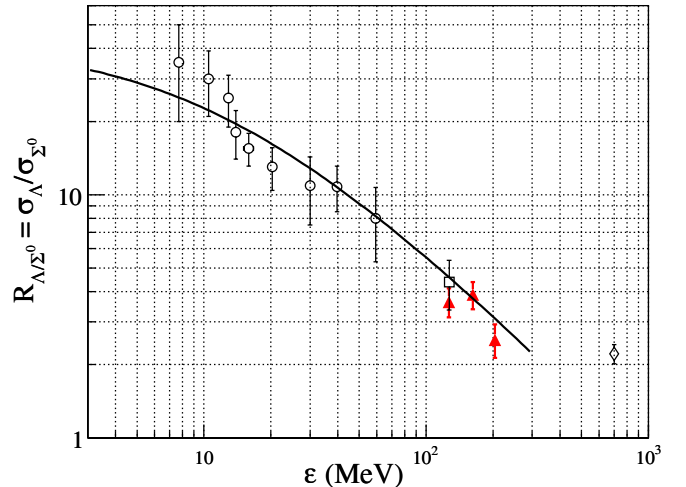
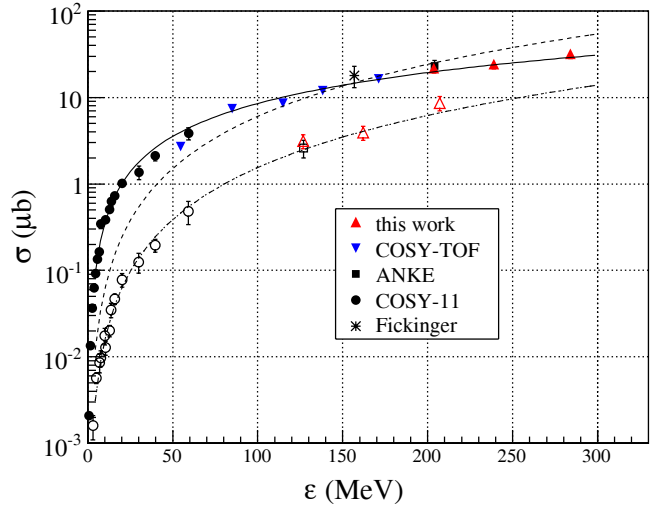


Fig. 4. Upper part: the world data set on total cross-sections of $pp \rightarrow pK^+\Lambda$ (solid symbols) and $pp \rightarrow pK^+\Sigma^0$ (open symbols) [1–7, 47]; dashed lines: phase space, solid line: phase space + FSI. Lower part: energy dependence of the cross-section ratio R_{Λ/Σ^0} . The open diamond at $\epsilon = 700$ MeV is an average value calculated from the data given in [8]. The results of the present work are shown as triangles. The solid line is the ratio of the parametrizations of the two excitation functions.

excitation function $\sigma_{\Sigma^0} = \sigma_{\Sigma^0}(\epsilon)$ is very well described within the experimental resolution by a pure phase-space dependence given by $\sigma_{pK^+\Sigma^0} = K \cdot \epsilon^2$ ($K = 1.545 \times 10^{-4} \mu\text{b}/\text{MeV}^2$, dash-dotted line in fig. 4).

The excitation function of $pp \rightarrow pK^+\Lambda$ clearly cannot be parameterized by pure phase space (dashed line in fig. 4). A parametrization proposed by Fäldt and Wilkin [48] is more appropriate

$$\sigma = C \cdot \frac{\epsilon^2}{(1 + \sqrt{1 + \epsilon/\alpha})^2} \quad (1)$$

and describes the energy dependence of the cross-section well up to 300 MeV (solid line in fig. 4; the parameters

$C = 0.02574 \mu\text{b}/\text{MeV}^2$ and $\alpha = 5.203 \text{ MeV}$ can be related to the $p\Lambda$ -FSI).

In the lower part of fig. 4 the ratio of both parametrizations is shown as a solid line together with the world data on cross-section ratios [3, 5, 8]. At the excess energies of 127 MeV a data point is added which is determined from the measured σ_{Σ^0} cross-sections given in [7] and the σ_A parametrization (1). At the same energy and at 162 MeV our results (shown as triangles) are also included, where the σ_A parametrization (1) and our new cross-sections for σ_{Σ^0} are used.

The two experimental cross-sections of $pp \rightarrow pK^+\Lambda$ at $\epsilon = 204 \text{ MeV}$ and $pp \rightarrow pK^+\Sigma^0$ at $\epsilon = 207 \text{ MeV}$ are used to directly calculate the ratio of $R_{A/\Sigma^0} = 2.5 \pm 0.4$, as the phase-space volume differs by less than 3%. In this ratio systematic uncertainties of the two measurements partly cancel (see introduction). The new experimental value confirms the general trend towards the high-energy limit of 2.2, which has been determined experimentally for $\epsilon > 700 \text{ MeV}$ in the 1960s and 1970s. At an excess energy of 204 MeV R_{A/Σ^0} is found to be more than one standard deviation below the value of three which follows from isospin considerations, and thus, this reasoning is unlikely to be the proper approach to explain the Λ to Σ^0 cross-section ratio.

Obviously, the energy region of enhanced Λ over Σ^0 production ends at excess energies of slightly above $\epsilon \approx 200 \text{ MeV}$. This surely is a surprise and will have implications on theory as for example the calculations of [10] predict values of $R_{A/\Sigma^0} \approx 5$ at $\epsilon = 200 \text{ MeV}$ and must be reconciled with the present finding. The same authors, however, point out that the total cross-sections for hyperon production are not sufficient to tightly constrain the parameters of any model. Therefore, differential distributions will be presented next.

3.2 Differential distributions: $pp \rightarrow pK^+\Lambda$

Differential data for the reaction $pp \rightarrow pK^+\Lambda$ are presented in figs. 5–9. In the one-dimensional differential distributions, data points are included as long as the uncertainty (quadratic sum of statistical error, the uncertainty of signal integration and acceptance correction) in a specific bin is below 80% of its cross-section value. In order to base the discussion on a quantitative footing, all one-dimensional distributions have been subjected to a least square fitting with Legendre polynomials $d\sigma/d\Omega = \sum_{l=0}^{l_{\max}} a_l \cdot P_l$, $l = 0, 1, 2, 4$. The coefficients are listed in the respective tables 2 to 4 and will be used only to judge anisotropies (P_2 and P_4) and asymmetries (P_1 , representative for all P_{odd}). The energy dependence of the observable under study can also be inferred and is found to be, in general, rather weak. It should be noted in passing that the total cross-section given by the integral of each differential distribution ($\sigma_{tot} = \int \frac{d\sigma}{d\Omega} d\Omega = 4\pi \cdot a_0$) in all cases is compatible within uncertainty with the values listed in table 1. The results obtained from (filtered) Monte Carlo data and the detector acceptance will be shown where appropriate.

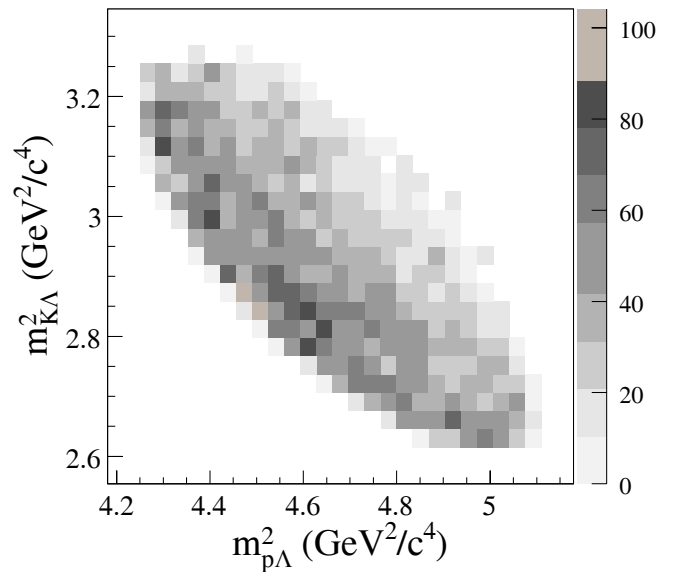


Fig. 5. Dalitz plot of the $pK^+\Lambda$ final state measured at $\epsilon = 204 \text{ MeV}$. The data is acceptance corrected, however, the background is not subtracted (see text). The scale of the relative bin occupancy is shown at the right side.

3.2.1 Dalitz plots

The acceptance-corrected Dalitz plot ($m_{K\Lambda}^2$ vs. $m_{p\Lambda}^2$) of the $pK^+\Lambda$ final state is shown in fig. 5 for an excess energy of 204 MeV ($p_{beam} = 2950 \text{ MeV}/c$). Data is shown for a missing-mass region of $\pm 50 \text{ MeV}/c^2$ around the Λ mass, hence reducing the contribution of background and Σ^0 hyperons. The plot is not corrected for background, however, sideband cuts below the Λ mass have been checked and show the background not to be responsible for the structures seen.

The relative bin occupancy of the Dalitz plot shown in fig. 5 resembles strongly the one presented in [6], which was determined for a smaller excess energy of $\epsilon = 171 \text{ MeV}$ ($p_{beam} = 2850 \text{ MeV}$). In both cases the kinematically allowed region is covered, an enhancement of the data is apparent along the lower $p\Lambda$ mass boundary, and no prominent resonant band is observed along the $m_{p\Lambda}^2$ -axis. This signature is explained in [6] by means of a quantitative Dalitz plot analysis. It was found that the nucleon resonances $N(1650)$, $N(1710)$, and $N(1720)$ in conjunction with a sizable $p\Lambda$ FSI play a decisive role, however, both are strongly interrelated by interference effects. A detailed analysis of a series of Dalitz plots measured at excess energies of 204, 284, and 316 MeV is the subject of a recent publication of the COSY-TOF Collaboration [49].

The present paper, hence, does not aim at an analysis of the Dalitz plot. We rather focus on presenting and discussing sets of one-dimensional differential distributions which have not been published so far. Our results substantially complement as well as support the earlier Dalitz plot analysis of [6].

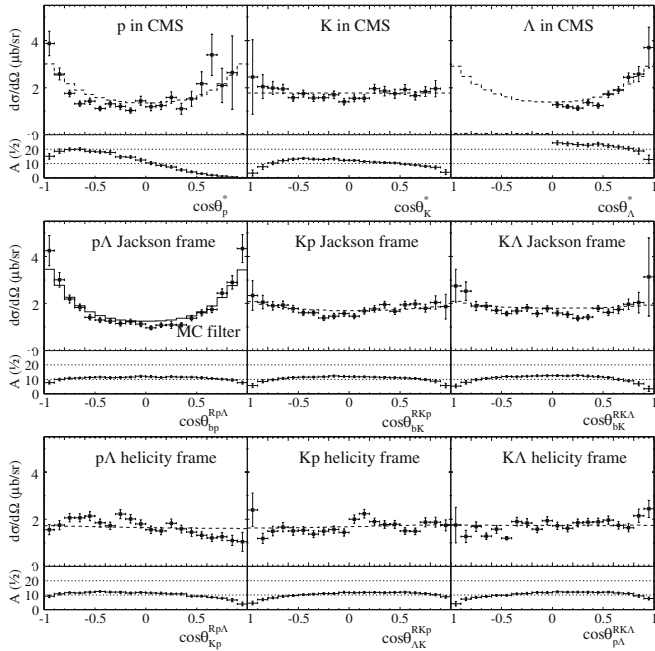


Fig. 6. Angular distributions of the particles in the overall CMS, Jackson and helicity frames (top-down) for the reaction $pp \rightarrow pK^+\Lambda$ measured at an excess energy of $\epsilon = 204$ MeV ($p_{beam} = 2950$ MeV/c). Error bars for each data point are the square root of the quadratic sum of the statistical, acceptance, and signal-to-background-separation uncertainty. The solid histogram in the $p\Lambda$ Jackson frame represents the Legendre polynomial of table 2 which is used as MC filter. Its effect on all other angular distributions is shown by the dashed histograms. Below each angular distributions the differential acceptance is shown.

3.2.2 Angular distributions in the overall CMS

The angular distributions of the three ejectiles in the overall CMS are shown in the upper row of figs. 6–8. The dashed histograms shown in the same pictures correspond to filtered Monte Carlo data and will be explained in detail in the following section. The change of acceptance is smooth as shown below each distribution. The steep decline of acceptance towards $\cos\theta = 1$ in the case of the kaon and proton distributions is caused by the requirement of evaluating only hyperons emitted into the forward CMS hemisphere. Nevertheless, the angular distributions of proton and kaon are symmetric with respect to $\cos\theta = 0$ as the coefficients a_1 in table 2 to 4 are compatible with zero. This symmetry in the overall CMS is mandatory in the case of identical particles in the entrance channel.

The angular distributions of protons and Λ hyperons show a pronounced anisotropy. The proton distributions even require the inclusion of P_4 . These anisotropies reflect relative angular momentum, L , in both the $p-(K^+\Lambda)$ and $\Lambda-(K^+p)$ system. From an inspection of the Legendre polynomial coefficients a_l in tables 2 to 4 one deduces ($L \leq 2$) for the former and ($L \leq 1$) for the latter. In contrast, the angular distributions of the kaons are essentially isotropic with a_2 coefficients deviating slightly from zero

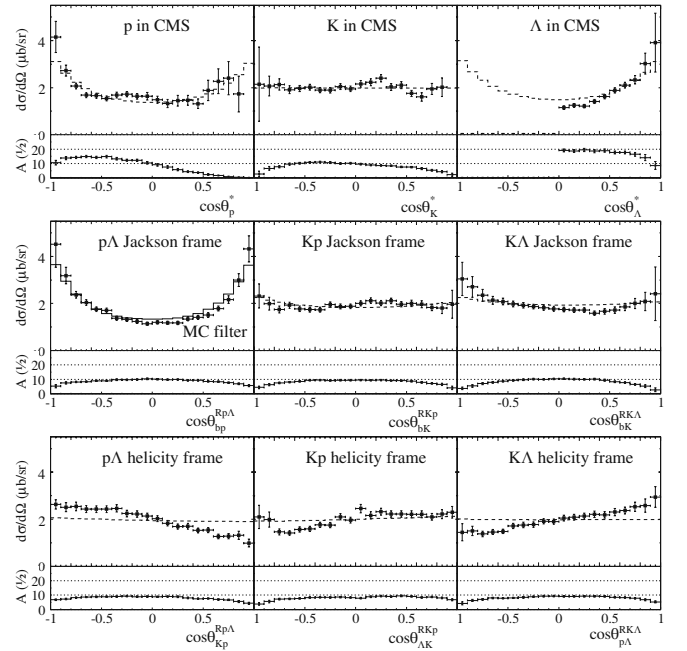


Fig. 7. Angular distributions of the particles in the overall CMS, the Jackson and helicity frames (top-down) for the reaction $pp \rightarrow pK^+\Lambda$ measured at an excess energy of $\epsilon = 239$ MeV ($p_{beam} = 3059$ MeV/c). Error bars for each data point are the square root of the quadratic sum of the statistical, acceptance, and signal-to-background-separation uncertainty. The solid histogram in the $p\Lambda$ Jackson frame represents the Legendre polynomial of table 3 which is used as MC filter. Its effect on all other angular distributions is shown by the dashed histograms. Below each angular distributions the differential acceptance is shown.

only for the two lower energies. This indicates relative angular momentum in the $K^+-(p\Lambda)$ system, if at all present, to become of even minor importance with increasing excess energy.

The three CMS angular distributions are compatible with each other simply due to kinematics. If the $K^+\Lambda$ system is assumed, as working hypothesis, to form an N^* -resonance the angular distribution of N^* is the mirror image of that of the associated proton. The N^* -resonance decays in its own rest frame back to back into hyperon and kaon. The available energy in this two-body decay depends on the mass of the resonance and may vary between zero and ϵ . However, due to the phase-space volume, it will mainly be at intermediate excess energies, *i.e.* in the order of 100 MeV. Kinematics then constrains the (heavier) hyperon to mainly preserve the direction of flight of the N^* -resonance, while the (lighter) kaon can be emitted isotropically. This kinematic situation holds also true if the N^* -resonance has a very large width; then the kinematics becomes similar to that of particles distributed homogeneously according to three-body phase space.

Thus, the angular distributions in the overall CMS are not well suited to directly draw conclusions on resonant or non-resonant production, as the former always displays a convolution of a two-step process ($pp \rightarrow pN^*$,

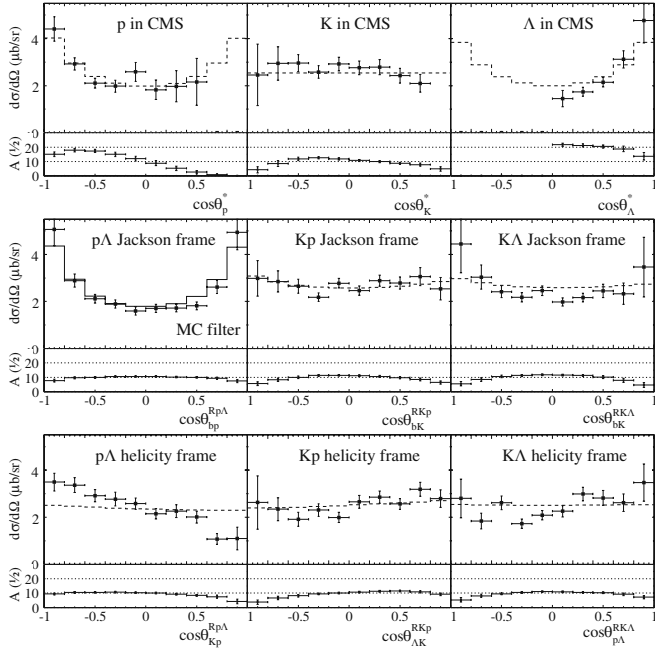


Fig. 8. Angular distributions of the particles in the overall CMS, the Jackson and helicity frames (top-down) for the reaction $pp \rightarrow pK^+\Lambda$ measured at an excess energy of $\epsilon = 284$ MeV ($p_{beam} = 3200$ MeV/c). Error bars for each data point are the square root of the quadratic sum of the statistical, acceptance, and signal-to-background-separation uncertainty. The solid histogram in the $p\Lambda$ Jackson frame represents the Legendre polynomial of table 4 which is used as MC filter. Its effect on all other angular distributions is shown by the dashed histograms. Below each angular distributions the differential acceptance is shown.

$N^* \rightarrow K^+\Lambda$). It will be shown in the following that Jackson and helicity frames are the much more natural choice of Lorentzian frames in order to study the reaction properties due to intermediate resonances.

3.2.3 Angular distributions in Jackson frames

The motivation for an analysis within Jackson frames², introduced by Gottfried and Jackson as early as 1964 [51], arises by considering the $\pi p \rightarrow KY$ vertex in fig. 1b,c to represent an isolated “2 → 2” reaction (the following argumentation is similar for the $Kp \rightarrow Kp$ vertex in fig. 1a).

² For reactions of type $ab \rightarrow 123$ the Jackson frame is defined as the Lorentzian frame in which the center of mass of the particles (2, 3) is at rest ($\mathbf{p}_3 = -\mathbf{p}_2$). In this frame the Jackson angle is defined as the angle between the beam direction and that of particle 3, *i.e.* $\triangle(\mathbf{p}_b, \mathbf{p}_3)$. This frame connects exit and entrance channel and carries information not accessible by means of a Dalitz plot analysis. In a three-body final state three two-body subsystems can be used to define a Jackson frame ($R23$, $R31$, $R12$; R indicating the Rest frame). The nomenclature of [50] is adopted: for θ_{b3}^{R23} the superscripts denotes the rest frame under consideration, the subscripts indicate the angle of particle 3 with respect to the beam b .

Table 2. Coefficients of Legendre polynomials (in units of $\mu\text{b}/\text{sr}$) determined by least-square fitting to angular distributions of the reaction $pp \rightarrow pK^+\Lambda$ at $\epsilon = 204$ MeV ($p_{beam} = 2950$ MeV/c).

cos	a_0	a_1	a_2	a_4
θ_p^*	$1.87 \pm .12$	$0.40 \pm .19$	$1.85 \pm .34$	$0.78 \pm .26$
θ_K^*	$1.76 \pm .06$	$0.04 \pm .10$	$0.37 \pm .16$	—
θ_Λ^*	$1.78 \pm .08$	—	$1.36 \pm .18$	—
θ_{bp}^{RpA}	$1.77 \pm .06$	$-0.00 \pm .10$	$1.59 \pm .14$	—
θ_{bK}^{RKp}	$1.79 \pm .04$	$0.10 \pm .08$	$0.50 \pm .12$	—
θ_{bK}^{RKA}	$1.76 \pm .05$	$-0.11 \pm .08$	$0.45 \pm .13$	—
θ_{Kp}^{RpA}	$1.64 \pm .04$	$-0.49 \pm .08$	$-0.32 \pm .11$	—
θ_{AK}^{RKp}	$1.61 \pm .04$	$0.22 \pm .08$	$-0.14 \pm .11$	—
θ_{pA}^{RKA}	$1.62 \pm .04$	$0.46 \pm .08$	$-0.16 \pm .13$	—

Table 3. Coefficients of Legendre polynomials (in units of $\mu\text{b}/\text{sr}$) determined by least-square fitting to angular distributions of the reaction $pp \rightarrow pK^+\Lambda$ at $\epsilon = 239$ MeV ($p_{beam} = 3059$ MeV/c).

cos	a_0	a_1	a_2	a_4
θ_p^*	1.94 ± 0.12	$-0.16 \pm .15$	$1.31 \pm .35$	$0.90 \pm .26$
θ_K^*	1.94 ± 0.05	$-0.01 \pm .09$	$-0.25 \pm .14$	—
θ_Λ^*	1.92 ± 0.08	—	$1.54 \pm .19$	—
θ_{bp}^{RpA}	1.86 ± 0.05	$-0.17 \pm .09$	$1.47 \pm .12$	—
θ_{bK}^{RKp}	1.89 ± 0.04	$0.14 \pm .07$	$-0.11 \pm .10$	—
θ_{bK}^{RKA}	1.96 ± 0.05	$-0.33 \pm .08$	$0.46 \pm .13$	—
θ_{Kp}^{RpA}	1.95 ± 0.03	$-0.87 \pm .06$	$-0.16 \pm .08$	—
θ_{AK}^{RKp}	1.91 ± 0.03	$0.56 \pm .06$	$-0.28 \pm .10$	—
θ_{pA}^{RKA}	1.96 ± 0.04	$0.70 \pm .07$	$-0.01 \pm .10$	—

In this picture, the inverse reaction ($KY \rightarrow p\pi$) must have the same properties due to time reversal invariance. If one now imagines colliding beams of kaons and hyperons with $\mathbf{p}_Y = -\mathbf{p}_K$, which is by definition the KY Jackson frame, it is self-evident that the distribution of angles θ_{bK}^{RKY} of the (in this case emerging) proton with respect to the (in this case beam-axis defining) kaon directly gives information on the relative angular momenta involved. This argumentation holds with or without an intermediate nucleon resonance.

Considering only this vertex four different particles are involved and, hence, the angular distributions are not at all restricted to show any symmetry with respect to

Table 4. Coefficients of Legendre polynomials (in units of $\mu\text{b}/\text{sr}$) determined by least-square fitting to angular distributions of the reaction $pp \rightarrow pK^+\Lambda$ at $\epsilon = 284 \text{ MeV}$ ($p_{beam} = 3200 \text{ MeV}/c$).

cos	a_0	a_1	a_2	a_4
θ_p^*	$2.74 \pm .52$	$-0.19 \pm .76$	2.29 ± 1.45	1.54 ± 1.18
θ_K^*	$2.55 \pm .18$	$-0.35 \pm .31$	-0.49 ± 0.50	—
θ_Λ^*	$2.61 \pm .28$	—	2.49 ± 0.74	—
θ_{bp}^{RpA}	$2.60 \pm .19$	$-0.19 \pm .33$	2.16 ± 0.43	—
θ_{bK}^{RKp}	$2.67 \pm .12$	$0.25 \pm .23$	0.25 ± 0.33	—
θ_{bK}^{RKA}	$2.59 \pm .18$	$-0.28 \pm .28$	0.97 ± 0.44	—
θ_{Kp}^{RpA}	$2.34 \pm .10$	$-1.37 \pm .20$	-0.23 ± 0.24	—
$\theta_{\Lambda K}^{RKp}$	$2.44 \pm .12$	$0.65 \pm .24$	0.17 ± 0.35	—
$\theta_{p\Lambda}^{RKA}$	$2.48 \pm .15$	$0.73 \pm .25$	0.65 ± 0.45	—

$\cos \theta_{bK}^{RKA} = 0$. In fact, $\pi^- p \rightarrow K^0 \Lambda$ scattering shows a strong anisotropy which can be traced back to the interference of resonances with opposite parity [52, 53]. Of course, the concept of an analysis within a Jackson frame is based on the presumption that there is no difference between a free and a virtual pion, and the form factor entering the $\pi p \rightarrow KY$ vertex is the same for both the two-body and the three-body reaction $pp \rightarrow pKY$ with no influence of the additional proton in the latter case.

A peculiarity arises in our case from the fact that the entrance channel consists of identical particles which results in symmetric angular distributions in the overall CMS in which beam and target are collinear. However, this collinearity is destroyed when the system is boosted into a Jackson frame (the angle between the two protons is $\approx 160^\circ$ on average). As beam and target particle are indistinguishable, the reference axis for the Jackson angle can be the direction of either proton. Therefore, the quantum mechanical identity of beam and target proton enforces the *same* angular distributions in the Jackson frame, when measured with respect to either proton. However, as a Jackson frame is some other Lorentzian frame than the CM system, the distributions are not required to show *any* symmetry.

The angular distributions in the Jackson frames are shown in the middle rows of figs. 6 to 8. As the two protons of the initial state cannot be distinguished, both Jackson angles with respect to beam and target have been taken into account for each event (maintaining for simplicity the subscript b in θ_{b3}^{R23}).

A pronounced anisotropy is observed in the $p\Lambda$ Jackson frame which is due to a relative angular momentum of $L = 1$ in the $p\Lambda$ system (see table 2 to 4). This anisotropy as well as those of the angular distributions of protons and Λ hyperons in the overall CMS suggest their connection through kinematics. In order to investigate this

conjecture all distributions measured in the CMS and the Jackson frames were used as weight functions for Monte Carlo simulations. It was found that solely the filter on the distribution in the $p\Lambda$ Jackson frame (solid histogram in figs. 6 to 8) results in a consistent and satisfactory description of all CMS distributions, illustrated by the dashed histograms. It is concluded that the resonance reaction $pp \rightarrow pN^*$ with angular momentum in this “exit” channel is of importance. The pN^* rest frame (which coincides with the CMS) is well represented by the $p\Lambda$ Jackson frame, due to the large mass difference of kaon and hyperon. Hence the $p\Lambda$ Jackson frame is the natural reference frame to study the dynamics of the intermediate pN^* system. It should be stressed that this information on angular momentum ($L \leq 2$) in the $p-N^*$ system is accessible neither by inspecting the CMS distributions nor the Dalitz plot. It is explicitly the choice of the respective Jackson frame which enables one to identify this aspect of the reaction dynamics.

The angular distributions in the K^+p Jackson frame are expected to be basically isotropic if the reaction proceeds in two steps via an intermediate N^* -resonance as the final-state protons and kaons do not originate from the same vertex (cf. figs. 1b,c) and are correlated only through kinematics of the final state. If, however, kaon exchange as indicated in fig. 1a plays an important role the distribution in the K^+p Jackson frame could reflect properties of that process which may even involve a yet unknown intermediate pentaquark resonance. The experimental angular distributions are symmetric within the experimental uncertainties (cf. a_1 coefficients in tables 2 to 4). There is a clear tendency for the coefficient a_2 to decrease with increasing excess energy pointing at an angular momentum L of at most one unit to be present in the K^+p interaction at smaller excess energy while L tends towards zero at higher excess energies. The Monte Carlo angular distributions resulting from the filter applied in the $p\Lambda$ Jackson frame reproduce the data quite well. This is taken as evidence for a kinematical correlation rather than a strong indication for kaon exchange, which, however, cannot be excluded to contribute at some level. In fact, Balestra *et al.* [54] concluded from negative spin transfer coefficients D_{NN} , measured in exclusive Λ production from $p\bar{p}$ collisions at $3.67 \text{ GeV}/c$, kaon exchange to contribute to the reaction mechanism in conjunction with pion exchange and Λp final-state interaction.

The experimental angular distributions in the $K^+\Lambda$ Jackson frame tend to be both anisotropic and asymmetric. Both effects are only poorly reproduced by filtered phase-space Monte Carlo data. It is thus tempting to assume these angular distributions to be caused by the excitation of N^* -resonances decaying into the $K^+\Lambda$ channel. All these nucleon resonances have large widths and may contribute through their broad tails to the reaction, even if their central mass is outside the mass region between the threshold ($1609 \text{ MeV}/c^2$) and $1893 \text{ MeV}/c^2$ (for the highest excess energy). An inspection of [25] reveals a long list of possibly participating N^* -resonances, classified as either S_{11} , P_{11} , P_{13} , D_{13} , D_{15} , or F_{15} . A Δ^* -resonance

cannot contribute due to isospin conservation. The coefficients of table 2 to 4 show a_1 to have a tendency to be non-zero while a_2 is non-zero. The fact that the inclusion of Legendre polynomials up to P_2 suffices for a good description shows that only angular momenta of $L \leq 1$ are participating in this “2→2 reaction” or, in other words, if N^* -resonances are involved their decay angular momentum must be $L \leq 1$. This constrains the resonances possibly involved to S_{11} , P_{11} , and P_{13} , where $L = 0$ belongs to the former, $L = 1$ to the latter two. Contributions of D_{13} , D_{15} , or F_{15} resonances, which would require $L > 1$, are therefore not supported by the data.

The angular distribution of a true two-body resonance reaction is asymmetric ($a_1 \neq 0$) only if resonances with both parities are simultaneously excited through interfering amplitudes [55] —this is observed in $\pi^- p \rightarrow K^0 \Lambda$ scattering [52, 53]. Hence, this distribution in the $K^+ \Lambda$ Jackson frame is a strong indication in the present analysis of one-dimensional distributions that more than one N^* -resonance with opposite parity participates in the production process, namely $N(1650)S_{11}$, $N(1710)P_{11}$, and $N(1720)P_{13}$. This section is concluded by stressing that this finding is fully consistent with that extracted from the Dalitz plot [6] which describes the correlations of the exit channel only.

3.2.4 Angular distributions in helicity frames

In a reaction of type $ab \rightarrow 123$ the helicity angle in a respective helicity frame³ interrelates the three particles of the exit channel; in fact, the helicity angle distribution is simply a special type of projection of a Dalitz plot. A uniformly populated Dalitz plot corresponds to isotropic helicity angle distributions whereas all physical and/or kinematical effects distorting the Dalitz plot must result in characteristic distributions in helicity frames. For example, an isolated narrow resonance decaying into the (23) system manifests itself as a “band” extending along the m_{13}^2 (or likewise m_{12}^2) axis in a Dalitz plot. The properties of mass and width of the resonance are seen in the (12) and (13) helicity frames while the decay pattern characteristic for the angular momentum of the resonance shows up in the (23) helicity frame.

The final-state interaction also distorts a Dalitz plot and consequently FSI effects are also seen in helicity angle distributions. A strong FSI, for example, between particle 1 and 3 leads to an enhancement at $\cos \theta_{13}^{R23} = 1$ and

³ For reactions of type $ab \rightarrow 123$ the helicity frame is defined as the Lorentzian frame in which the center of mass of the particles (2,3) is at rest ($\mathbf{p}_3 = -\mathbf{p}_2$), *i.e.* it is the identical Lorentzian frame as the respective Jackson frame. The choice of the word “frame” relates to the reference axis, which in case of the helicity frame is the direction of particle 1. As in the case of Jackson frames, three helicity frames can be constructed by cyclic permutation for the three-body final state ($R23$, $R31$, $R12$). Nomenclature: θ_{13}^{R23} is the angle of particle 3 with respect to the reference axis 1 (subscript), measured in the rest frame of particle 2 and 3 (superscript).

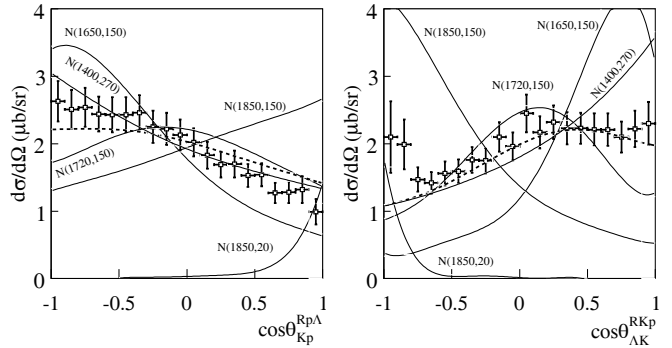


Fig. 9. Angular distributions measured in the $p\Lambda$ (left panel) and $K^+ p$ (right panel) helicity frames. The lines are the Monte Carlo result for various nucleon resonances ($N(m, \Gamma)$). The dashed line is the result for an incoherent sum of Monte Carlo data (see text).

$\cos \theta_{32}^{R12} = -1$. If, however, FSI effects and various (resonant and non-resonant) reaction mechanisms contribute the situation becomes by far more complicated and quantitative conclusions can only be drawn with caution. Then, theoretical models have to treat all contributions in a coherent manner and their results have to be confronted with the data. Such an approach was adopted for the $pp \rightarrow pK^+ \Lambda$ channel and an excess energy of 130 MeV by Sibirtsev *et al.* [56]. These authors pointed out that helicity distributions are ideally suited to determine the various contributions to the reaction mechanism in a quantitative manner.

The angular distributions in the three helicity frames are shown in the lower rows of figs. 6 to 8. All distributions deviate significantly from isotropy. The dashed histograms, which are isotropic, again are the results of Monte Carlo data filtered with the experimental distribution as measured in the $p\Lambda$ Jackson frame. The filter is without any effect on the helicity angle as the latter is solely an exit channel property. The parameters of Legendre polynomial fittings to the experimental distributions are shown in tables 2 to 4.

As mentioned above, the distributions in helicity frames both depend on and reflect, via kinematics, the masses and the widths of participating nucleon resonances. In order to stress these aspects, the experimental data taken at $\epsilon = 239$ MeV are shown in fig. 9 again, in the $p\Lambda$ (left-hand side), in the $K^+ p$ (right-hand side) helicity frames. In the same pictures are included the results of Monte Carlo simulations of single nucleon resonances ($N^* \rightarrow K^+ \Lambda$) with mass m and width Γ abbreviated as $N(m, \Gamma)$. In addition, the result for an incoherent sum of three Monte Carlo data-sets (phase space, $N(1650, 150)$, $N(1720, 150)$ —all entering with equal weight) is shown as a dashed line. Some general conclusions will now be drawn by comparing these Monte Carlo distributions with the measured ones.

The effect of narrow resonances ($N(1600)$, $N(1650)$, $N(1720)$, $N(1850)$; $\Gamma = 20$ MeV) is studied first; they were found to cause strongly localized distortions of the

distributions in both helicity frames. As an example the result for $N(1850, 20)$, assumed to have a cross-section of $2.5 \mu\text{b}$, is shown in fig. 9. In this case the distribution in the K^+p helicity frame would leave room for such a resonance to contribute, however the corresponding characteristic distortion in the $p\Lambda$ helicity frame is not observed experimentally. The results obtained for all the other narrow resonances are incompatible with the data in both frames. Hence, any hypothetical narrow resonance (“missing” or exotic) is excluded to contribute on a level of about $2.5 \mu\text{b}$.

Resonances with masses $m_{N^*} \geq 1850 \text{ MeV}$ and various widths of $\Gamma = 150\text{--}400 \text{ MeV}$ yield distributions incompatible with the measured ones. As an example for this class of resonances, the effect of the $N(1850, 150)$ is shown in fig. 9. The distributions of measured and Monte Carlo data clearly show opposite slopes in either frame. Thus a whole set of resonances, namely $N(1900)P_{13}$ [25], $N(1840)P_{11}$ [26], $N(1875)D_{13}$ [26], $N(1895)D_{13}$ [27, 28], and $N(1950)D_{13}$ [29] is unlikely to contribute to the reaction $pp \rightarrow pK^+\Lambda$.

The kinematical effect of a light nucleon resonance was studied by means of a simulation of an $N(1400, 270)$ -resonance. As its central mass is smaller than the sum of the masses of kaon and Λ the production process can only proceed via the broad tail of the resonance. The numerical values for mass and width are chosen according to the result of the resonance isobar model of ref. [12] which explains well the energy dependence of the ratio R_{Λ/Σ^0} by invoking only this resonance. The distributions generated by this single resonance follow fairly well the experimental one in the $p\Lambda$ but fail to produce that observed in the Kp helicity frame. Hence, a broad sub-threshold resonance alone is not able to account for the kinematic situation found in the $pK^+\Lambda$ final state.

The same observation holds true for both $N(1650, 150)$ and $N(1720, 150)$ which on their own are not able to describe the observed angular distributions in fig. 9. Similarly, a distribution according to pure three-body phase does not follow the data as it leads to isotropic distributions (not shown). On the other hand, the sum of these two resonances and phase space (represented by the dashed line) follows the experimental data very well. Of course, this mere incoherent superposition reflects only a particular kinematic situation (omitting FSI effects) and does not describe the dynamics of the $pK^+\Lambda$ production process. Therefore, beyond kinematics, it should be interpreted with caution, especially as the analysis of distributions in the $K^+\Lambda$ Jackson frame strongly indicated interference effects due to resonances with certain spins and opposite parity, namely S_{11} , P_{11} , and P_{13} . These are just the states $N(1650)S_{11}$, $N(1710)P_{11}/N(1720)P_{13}$ which were included in the Monte Carlo simulation. Thus, the very good reproduction of the experimental data by a curve resulting from an incoherent sum of three Monte Carlo data sets supports, from a kinematical point of view, that the resonances involved are, indeed, $N(1650)S_{11}$, $N(1710)P_{11}/N(1720)P_{13}$.

Finally, the implications of the $p\Lambda$ helicity angle distributions for the explanation of the Λ to Σ^0 cross-section ratio near the threshold are discussed. In [9] $R_{\Lambda/\Sigma^0} = 27$ was predicted from the ratio of the KNY coupling constants $g_{N\Lambda K}^2/g_{N\Sigma K}^2$. Obviously, for this prediction to apply the production process must be dominated by kaon exchange (fig. 1a). Pure kaon exchange, however, should lead to an isotropic distribution in the $p\Lambda$ helicity frame [56], which is not observed experimentally. Hence, kaon exchange cannot be the dominant production process and nucleon resonances have also to be taken into account at the excess energies considered here. Then it is reasonable to assume that resonant contributions are also present near the threshold, as, *e.g.*, the $N(1650)S_{11}$ -resonance (width $\approx 165 \text{ MeV}$ [25]) can easily be produced at threshold energies. Hence, the explanation of the R_{Λ/Σ^0} to be solely related to the KNY coupling constants is not likely to be correct.

The angular distributions in the $K^+\Lambda$ helicity frame are shown in the lower-right frames of figs. 6 to 8. An apparent enhancement towards $\cos \theta_{p\Lambda}^{RKA} = 1$ is observed for all excess energies. This asymmetry cannot be caused by any single nucleon resonance, as in this case the distribution would be either isotropic (decay angular momentum $L = 0$) or symmetric with respect to $\cos \theta = 0$ ($L \geq 1$).

The $p\Lambda$ FSI introduces an asymmetry with enhanced cross-section towards $\cos \theta_{p\Lambda}^{RKA} = 1$. However, FSI effects are limited to relative energies of the $p\Lambda$ system of just a few MeV and therefore influence only a limited region of the Dalitz plot at the excess energies considered here. Thus, it is difficult to see how the observed asymmetric distribution in the $K^+\Lambda$ helicity frame, which is a projection of the whole Dalitz plot, can be explained solely by FSI. If one excludes exotic resonances decaying into the $p\Lambda$ or pK^+ channel, which would lead via kinematics to an asymmetry in the $K^+\Lambda$ helicity frame, one is left with the conclusion that a coherent interference of various N^* -resonances (including FSI) dominates the reaction. It is known that the interference of resonances of different parity leads to asymmetric angular distributions [55]. The analysis of the distributions in the $K^+\Lambda$ Jackson frame evidenced that more than one resonance of opposite parity are involved. The discussion of fig. 9 showed that a combined contribution of the $N(1650)S_{11}$ and $N(1710)P_{11}/N(1720)P_{13}$, which have opposite parity, is kinematically supported. Hence, the mentioned interference of resonances with different parity is possible and likely to cause the asymmetry observed in the $K^+\Lambda$ helicity frame.

We like to end this section with a comment on a very recent observation of an exotic resonant state X ($m_X = 2267 \text{ MeV}/c^2$, $\Gamma_X = 118 \text{ MeV}/c^2$) which decays into two baryons, a non-strange proton and a strange Λ hyperon [57]. The resonance is interpreted to be a deeply bound, compact K^-pp cluster (binding energy $\approx 100 \text{ MeV}$) which, hence, could be a possible gateway towards cold and dense kaonic nuclear matter. The measurement was carried out with a beam momentum of $3670 \text{ MeV}/c$ which corresponds to an excess energy of

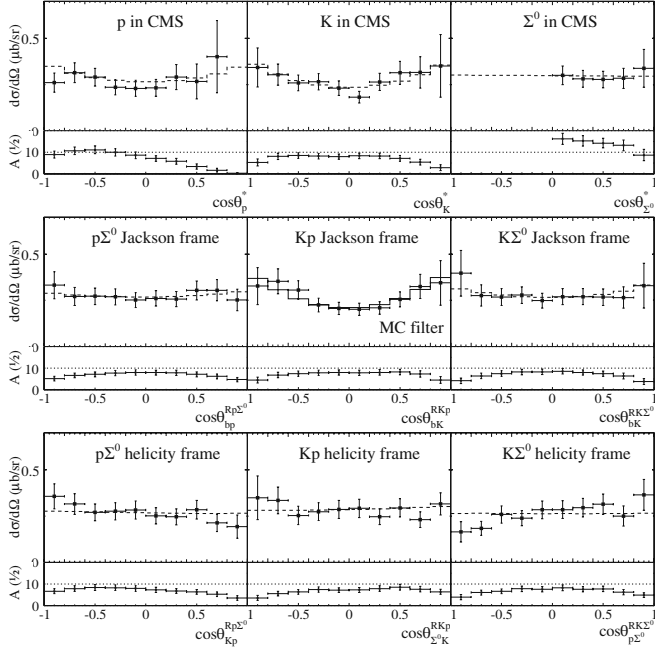


Fig. 10. Angular distributions of the particles in the overall CMS, Jackson and helicity frames (top-down) for the reaction $pp \rightarrow pK^+\Sigma^0$ measured at an excess energy of $\epsilon = 162$ MeV ($p_{beam} = 3059$ MeV/c). Error bars for each data point are the square root of the quadratic sum of the statistical, acceptance, and signal-to-background-separation uncertainty. The solid histogram in the Kp Jackson frame represents the Legendre polynomial of table 5 which is used as MC filter. Its effect on all other angular distributions is shown by the dashed histograms. Below each angular distributions the differential acceptance is shown.

$\epsilon = \sqrt{s} - m_{K^+} - m_X = 221$ MeV. At this energy, the contribution of this exotic K^+X production to the total $pp \rightarrow pK^+\Lambda$ cross-section is found to be about 20%.

Compared to [57] the beam momenta considered in this paper (2950, 3059, 3200 MeV/c) correspond to considerably smaller excess energies of -9, 26, and 71 MeV for K^+X production. Due to the width of the resonance the K^+X final state is kinematically accessible even at the negative excess energy of -9 MeV. However, all three excess energies are smaller than the width of the resonance. Thus, the strength of possible contributions must consequently be considerably smaller compared to [57]. Contributing only on a few percent level, such a weak signal is obviously difficult to observe directly in figs. 6-9. The theory is now asked to explore the benefit of adding this exotic state, in addition to “standard” nucleon resonances decaying into $K^+\Lambda$, when reproducing our data.

3.3 Differential distributions: $pp \rightarrow pK^+\Sigma^0$

The data set taken at $p_{beam} = 3059$ MeV/c ($\epsilon_\Sigma^0 = 162$ MeV) provides for the first time direct insight into the reaction dynamics of proton-proton-induced $pK^+\Sigma^0$

Table 5. Coefficients of Legendre polynomials (in units of $\mu\text{b}/\text{sr}$) determined by least-square fitting to angular distributions of the reaction $pp \rightarrow pK^+\Sigma^0$ at $\epsilon = 162$ MeV ($p_{beam} = 3059$ MeV/c).

\cos	a_0	a_1	a_2
θ_p^*	0.28 ± 0.04	0.03 ± 0.07	0.07 ± 0.08
θ_K^*	0.29 ± 0.02	0.01 ± 0.05	0.14 ± 0.06
$\theta_{\Sigma^0}^*$	0.29 ± 0.03	—	0.01 ± 0.07
$\theta_{bp}^{Rp\Sigma^0}$	0.27 ± 0.02	-0.00 ± 0.03	0.03 ± 0.04
θ_{bK}^{RKp}	0.28 ± 0.02	-0.02 ± 0.04	0.16 ± 0.05
$\theta_{bK}^{RK\Sigma^0}$	0.28 ± 0.02	-0.01 ± 0.04	0.04 ± 0.05
$\theta_{Kp}^{Rp\Sigma^0}$	0.27 ± 0.02	-0.06 ± 0.03	0.00 ± 0.04
$\theta_{\Sigma^0 K}^{RKp}$	0.28 ± 0.02	-0.03 ± 0.04	0.03 ± 0.05
$\theta_{p\Sigma^0}^{RK\Sigma^0}$	0.26 ± 0.02	0.07 ± 0.03	-0.04 ± 0.04

production as differential observables are accessible. These angular distributions are shown in fig. 10; the coefficients from the least-square fitting are listed in table 5. The histograms represent filtered Monte Carlo data, which will be explained in the course of the discussion. The arrangement within the figure is analogous to the case of Λ production (figs. 6 to 8), *i.e.* the first row shows distributions in the overall CMS while in the second and third row distributions in the Jackson and helicity frames are presented, respectively. In order to avoid repetition, we will draw on arguments presented above in order to directly deduce conclusions on $pK^+\Sigma^0$ production. Emphasis will be put on a comparison of both hyperon production channels closest in excess energy where, for the time being, the difference in $\epsilon_\Lambda = 204$ MeV and $\epsilon_\Sigma^0 = 162$ MeV is ignored. This seems justified as the reaction mechanism for Λ production was found, as shown above, not to change dramatically with excess energy.

The distributions in the overall CMS and the Jackson frames for Λ and Σ^0 production (first/second row in figs. 6 and 10) not only differ apparently but in addition show an opposite behavior. An inspection of the parameters given in table 5 shows that the proton and Σ^0 CMS distributions as well as the those in the $p\Sigma^0$ and $K^+\Sigma^0$ Jackson frame are compatible with isotropy whereas the corresponding distributions in the $pK\Lambda$ channel (table 2) show strong anisotropy; for the $pK\Lambda$ channel the kaon distribution in the CMS and that in the K^+p Jackson frame feature a pronounced anisotropy whereas the corresponding distributions in the Λ channel show strong isotropy. These finding are the first proof that the reaction mechanisms differ significantly for the reaction $pp \rightarrow pK^+\Lambda$ and $pp \rightarrow pK^+\Sigma^0$.

From the CMS distributions one directly concludes that the $K^+-(p\Sigma^0)$ system shows some indication of $L = 1$

while the Σ^0 hyperon has no relative angular momentum with respect to the pK^+ subsystem. This is in line with the mainly isotropic distribution observed in the $p\Sigma^0$ Jackson frame. Hence, if intermediate resonances are involved (N^* or Δ^*), the relative angular momentum shared by the p - N^* or p - Δ^* system is $L = 0$, remarkably different from the case of Λ production.

The fact that no angular momentum is involved in the p - N^*/Δ^* system signifies that only particular partial waves in the entrance channel can participate. The nuclear reaction theory developed by Blatt and Biedenharn [55] shows that isotropic angular distributions are only possible if one of the three following quantities is zero: entrance or exit channel angular momentum or total angular momentum. This condition is always fulfilled for the entrance channel states 1S_0 and 3P_0 , irrespectively of the final state involved. It is also met for 3P_1 if it produces S_{11} or S_{31} resonances in the exit channel. Thus, the observed isotropy significantly constrains partial waves being possible in entrance and exit channel. A conclusion like that could not be drawn in the case of the $pp \rightarrow pK^+\Lambda$ reaction as the corresponding angular distributions are anisotropic.

The distribution in the $K^+\Sigma^0$ Jackson frame shows isotropy within uncertainty. Hence, there is only little room for resonances with intrinsic angular momentum. Thus, from the list of nucleon resonances with assumed decay branches to $K^+\Sigma^0$ [25], the resonances to be possibly involved are most likely $N(1650)S_{11}$, and $\Delta(1900)S_{31}$ while $N(1710)P_{11}$, $N(1720)P_{13}$, and $\Delta(1750)P_{31}$ seem less probable to contribute.

The distribution in the K^+p Jackson frame shows anisotropy. This indicates that the proton-kaon subsystem carries a relative angular momentum of $L = 1$. This cannot be the decay angular momentum of N^* or Δ^* resonances as it is impossible for them to disintegrate into a non-strange proton and a strange kaon —only an as yet unknown pentaquark state could feature such a decay. The anisotropy observed is rather conjectured to be a strong indication of the presence of kaon exchange (fig. 1a). This again discriminates between the Σ^0 and the Λ channel.

As in the case of the Λ production a filter was set on those distributions which deviate the most from isotropy. It is found that the filter on the distribution in the Kp Jackson frame (solid-line histogram) is well suited to simultaneously describe the data in the CMS and Jackson frames (dashed-line histograms).

The distributions in the three helicity frames are presented in the bottom row of fig. 10. Compared to those for the Λ production shown in fig. 6 ($\epsilon = 204$ MeV) these distributions feature a smaller, however, still significant anisotropy. In particular, the asymmetric distribution in the $K^+\Sigma^0$ helicity frame show interference effects which, in the present case of Σ^0 production, may involve nucleon as well as Δ -resonances, kaon exchange potentially carrying angular momentum as well as all three possible final-state interactions.

3.4 Summary

Associated strangeness production was investigated in the reactions $pp \rightarrow pK^+\Lambda$ and $pp \rightarrow pK^+\Sigma^0$ using data collected by the time-of-flight spectrometer COSY-TOF. Data were analyzed for three different beam momenta ($p_{beam} = 2950, 3059, 3200$ MeV/c), which correspond to excess energies of 204, 239, and 284 MeV in the case of Λ production whereas the neutral Σ is produced 127, 162, and 207 MeV above the threshold.

These measurements extend the experimental knowledge of both reactions by roughly 80 MeV into an energy range formerly believed to show a sizable enhancement of the ratio of the Λ to Σ^0 cross-section. At $\epsilon = 204$ MeV this ratio is found to be 2.5 ± 0.4 and shows the high-energy limit, so far measured for $\epsilon > 700$ MeV, to be reached already in the region of the moderate excess energies considered here.

In the case of $pp \rightarrow pK^+\Lambda$ differential cross-sections were obtained in the CM, Jackson, and helicity frames for all three excess energies. Strong evidence was found for a production scenario including intermediate nucleon resonances. Especially a process which involves $N(1650)S_{11}$, $N(1710)P_{11}$, and/or $N(1720)P_{13}$ is deduced from the data; D_{13} , D_{15} , and F_{15} resonances are unlikely to contribute. Kaon exchange with angular momentum $L \geq 1$ is excluded while $L = 0$ may be present, however, surely not being the dominant process.

For the reaction $pp \rightarrow pK^+\Sigma^0$ the first differential data have been shown ($\epsilon = 162$ MeV). The distributions in the overall CMS as well as in the various Jackson frames feature an opposite behavior with respect to those observed for Λ production. Only entrance channel partial waves 1S_0 , 3P_0 , and 3P_1 are found to be involved. Strong indication is found for kaon exchange carrying angular momentum. If resonances contribute to Σ^0 production they are likely to be of the type S_{11} and S_{31} .

Thus, one of the key results of this paper is the proof that the reaction mechanisms for Σ^0 and Λ production differ decisively. With this differential data at hand theory is now challenged to advance a model which simultaneously describes the data presented.

The authors would like to express their gratitude to the COSY staff for the operation of the accelerator during the experiments. Discussions with V.A. Nikonorov, A.V. Sarantsev and A.A. Sibirtsev are gratefully acknowledged. This work was supported in part by grants from BMBF and Forschungszentrum Jülich (COSY-FFE).

Appendix A. Data tables

Tables 6–9 list the numerical values of all one-dimensional cross-sections.

Table 6. Cross-sections in $\mu\text{b}/\text{sr}$ for the reaction $pp \rightarrow pK^+\Lambda$, $p_{beam} = 2950 \text{ MeV}/c$, $\epsilon = 204 \text{ MeV}$, fig. 6.

$\cos \theta$	$\frac{d\sigma}{d\Omega}(\theta_p^*)$	$\frac{d\sigma}{d\Omega}(\theta_{K^+}^*)$	$\frac{d\sigma}{d\Omega}(\theta_\Lambda^*)$	$\frac{d\sigma}{d\Omega}(\theta_{bp}^{Rp\Lambda})$	$\frac{d\sigma}{d\Omega}(\theta_{bK}^{RKp})$	$\frac{d\sigma}{d\Omega}(\theta_{bK}^{RK\Lambda})$	$\frac{d\sigma}{d\Omega}(\theta_{Kp}^{Rp\Lambda})$	$\frac{d\sigma}{d\Omega}(\theta_{\Lambda K}^{RKp})$	$\frac{d\sigma}{d\Omega}(\theta_{p\Lambda}^{RK\Lambda})$
-0.95	3.88 ± 0.52	2.46 ± 1.58	—	4.25 ± 0.65	2.34 ± 0.63	2.75 ± 0.70	1.56 ± 0.22	2.40 ± 0.71	1.76 ± 0.75
-0.85	2.58 ± 0.25	2.04 ± 0.50	—	3.00 ± 0.31	2.06 ± 0.29	2.52 ± 0.39	1.75 ± 0.19	1.19 ± 0.22	1.27 ± 0.26
-0.75	1.75 ± 0.15	1.99 ± 0.28	—	2.19 ± 0.17	1.90 ± 0.18	1.89 ± 0.20	2.07 ± 0.18	1.50 ± 0.20	1.69 ± 0.20
-0.65	1.32 ± 0.12	1.94 ± 0.20	—	1.83 ± 0.14	1.94 ± 0.16	1.88 ± 0.15	2.06 ± 0.18	1.67 ± 0.19	1.28 ± 0.14
-0.55	1.42 ± 0.14	1.58 ± 0.15	—	1.42 ± 0.12	1.78 ± 0.14	1.71 ± 0.14	2.13 ± 0.19	1.50 ± 0.18	1.58 ± 0.17
-0.45	1.12 ± 0.10	1.75 ± 0.15	—	1.29 ± 0.10	1.61 ± 0.12	1.58 ± 0.10	1.85 ± 0.16	1.53 ± 0.16	1.20 ± 0.07
-0.35	1.31 ± 0.13	1.56 ± 0.14	—	1.25 ± 0.11	1.61 ± 0.11	1.68 ± 0.13	1.72 ± 0.15	1.37 ± 0.15	1.90 ± 0.18
-0.25	1.20 ± 0.13	1.58 ± 0.14	—	1.14 ± 0.11	1.38 ± 0.11	1.81 ± 0.14	2.22 ± 0.19	1.49 ± 0.16	1.84 ± 0.18
-0.15	1.03 ± 0.11	1.70 ± 0.16	—	1.22 ± 0.11	1.46 ± 0.12	1.57 ± 0.12	2.02 ± 0.18	1.57 ± 0.15	1.58 ± 0.15
-0.05	1.44 ± 0.19	1.40 ± 0.14	—	1.12 ± 0.10	1.57 ± 0.12	1.78 ± 0.13	1.80 ± 0.17	1.44 ± 0.15	1.94 ± 0.17
0.05	1.19 ± 0.17	1.55 ± 0.15	1.27 ± 0.12	0.97 ± 0.09	1.46 ± 0.11	1.59 ± 0.12	1.56 ± 0.16	2.01 ± 0.18	1.72 ± 0.16
0.15	1.24 ± 0.17	1.55 ± 0.15	1.20 ± 0.08	1.08 ± 0.10	1.69 ± 0.14	1.53 ± 0.12	1.50 ± 0.16	2.23 ± 0.19	1.62 ± 0.15
0.25	1.58 ± 0.24	1.96 ± 0.18	1.13 ± 0.10	1.09 ± 0.15	1.77 ± 0.14	1.37 ± 0.11	1.83 ± 0.18	1.90 ± 0.14	1.85 ± 0.17
0.35	1.10 ± 0.24	1.85 ± 0.20	1.36 ± 0.11	1.09 ± 0.10	1.95 ± 0.14	1.42 ± 0.11	1.59 ± 0.17	1.78 ± 0.16	1.88 ± 0.16
0.45	1.52 ± 0.32	1.74 ± 0.19	1.24 ± 0.11	1.38 ± 0.12	1.67 ± 0.14	1.79 ± 0.13	1.46 ± 0.19	1.79 ± 0.17	1.88 ± 0.17
0.55	2.16 ± 0.51	1.92 ± 0.21	1.72 ± 0.14	1.60 ± 0.13	1.95 ± 0.15	1.62 ± 0.14	1.32 ± 0.14	1.50 ± 0.14	1.96 ± 0.17
0.65	3.39 ± 0.88	1.66 ± 0.18	1.89 ± 0.15	1.74 ± 0.14	1.98 ± 0.16	1.75 ± 0.17	1.21 ± 0.15	1.49 ± 0.15	1.74 ± 0.16
0.75	2.09 ± 0.73	1.84 ± 0.21	2.44 ± 0.19	2.44 ± 0.19	1.80 ± 0.17	1.97 ± 0.23	1.26 ± 0.17	1.87 ± 0.19	1.64 ± 0.17
0.85	2.64 ± 1.56	1.96 ± 0.35	2.58 ± 0.32	2.90 ± 0.29	2.04 ± 0.29	2.04 ± 0.44	1.10 ± 0.22	1.88 ± 0.21	2.15 ± 0.28
0.95	—	—	3.70 ± 0.86	4.33 ± 0.59	1.86 ± 0.53	3.13 ± 1.66	1.04 ± 0.40	1.74 ± 0.23	2.44 ± 0.37

Table 7. Cross-sections in $\mu\text{b}/\text{sr}$ for the reaction $pp \rightarrow pK^+\Lambda$, $p_{beam} = 3059 \text{ MeV}/c$, $\epsilon = 239 \text{ MeV}$, fig. 7.

$\cos \theta$	$\frac{d\sigma}{d\Omega}(\theta_p^*)$	$\frac{d\sigma}{d\Omega}(\theta_{K^+}^*)$	$\frac{d\sigma}{d\Omega}(\theta_\Lambda^*)$	$\frac{d\sigma}{d\Omega}(\theta_{bp}^{Rp\Lambda})$	$\frac{d\sigma}{d\Omega}(\theta_{bK}^{RKp})$	$\frac{d\sigma}{d\Omega}(\theta_{bK}^{RK\Lambda})$	$\frac{d\sigma}{d\Omega}(\theta_{Kp}^{Rp\Lambda})$	$\frac{d\sigma}{d\Omega}(\theta_{\Lambda K}^{RKp})$	$\frac{d\sigma}{d\Omega}(\theta_{p\Lambda}^{RK\Lambda})$
-0.95	4.15 ± 0.66	2.15 ± 1.57	—	4.52 ± 0.98	2.32 ± 0.51	3.04 ± 0.70	2.63 ± 0.20	2.10 ± 0.50	1.45 ± 0.36
-0.85	2.72 ± 0.23	2.07 ± 0.42	—	3.19 ± 0.36	1.99 ± 0.27	2.70 ± 0.44	2.51 ± 0.20	1.99 ± 0.32	1.51 ± 0.20
-0.75	2.07 ± 0.12	2.13 ± 0.24	—	2.37 ± 0.15	1.74 ± 0.15	2.35 ± 0.25	2.54 ± 0.18	1.47 ± 0.13	1.38 ± 0.12
-0.65	1.68 ± 0.10	1.91 ± 0.17	—	2.04 ± 0.13	1.93 ± 0.13	2.14 ± 0.17	2.44 ± 0.15	1.42 ± 0.10	1.46 ± 0.10
-0.55	1.66 ± 0.10	1.97 ± 0.13	—	1.76 ± 0.10	1.77 ± 0.12	2.08 ± 0.14	2.43 ± 0.15	1.56 ± 0.11	1.49 ± 0.09
-0.45	1.54 ± 0.10	2.02 ± 0.12	—	1.70 ± 0.10	1.74 ± 0.10	1.98 ± 0.12	2.43 ± 0.14	1.59 ± 0.11	1.72 ± 0.11
-0.35	1.68 ± 0.12	1.89 ± 0.11	—	1.38 ± 0.08	1.74 ± 0.10	1.92 ± 0.11	2.46 ± 0.15	1.76 ± 0.11	1.76 ± 0.12
-0.25	1.73 ± 0.11	1.89 ± 0.12	—	1.32 ± 0.08	1.96 ± 0.11	1.87 ± 0.10	2.25 ± 0.14	1.75 ± 0.11	1.77 ± 0.11
-0.15	1.63 ± 0.12	2.05 ± 0.13	—	1.23 ± 0.07	1.87 ± 0.10	1.81 ± 0.10	2.22 ± 0.14	2.10 ± 0.13	1.91 ± 0.12
-0.05	1.64 ± 0.16	1.95 ± 0.12	—	1.14 ± 0.07	1.88 ± 0.10	1.77 ± 0.10	2.13 ± 0.13	1.96 ± 0.13	1.90 ± 0.11
0.05	1.49 ± 0.15	2.16 ± 0.14	1.16 ± 0.07	1.20 ± 0.07	2.01 ± 0.11	1.75 ± 0.10	2.02 ± 0.12	2.45 ± 0.18	2.05 ± 0.12
0.15	1.33 ± 0.17	2.23 ± 0.15	1.25 ± 0.08	1.18 ± 0.07	2.12 ± 0.12	1.72 ± 0.10	1.83 ± 0.11	2.17 ± 0.16	2.08 ± 0.12
0.25	1.45 ± 0.23	2.40 ± 0.15	1.22 ± 0.08	1.18 ± 0.07	2.02 ± 0.11	1.72 ± 0.10	1.69 ± 0.11	2.32 ± 0.14	2.13 ± 0.13
0.35	1.46 ± 0.21	2.03 ± 0.14	1.42 ± 0.09	1.34 ± 0.08	2.11 ± 0.12	1.58 ± 0.09	1.70 ± 0.13	2.23 ± 0.14	2.21 ± 0.13
0.45	1.32 ± 0.20	2.11 ± 0.15	1.62 ± 0.10	1.41 ± 0.09	1.97 ± 0.11	1.67 ± 0.12	1.53 ± 0.11	2.23 ± 0.13	2.19 ± 0.14
0.55	1.89 ± 0.43	1.75 ± 0.13	1.88 ± 0.11	1.51 ± 0.10	2.01 ± 0.13	1.72 ± 0.13	1.54 ± 0.11	2.21 ± 0.15	2.31 ± 0.15
0.65	2.27 ± 0.53	1.61 ± 0.18	2.10 ± 0.12	1.79 ± 0.11	1.97 ± 0.15	1.85 ± 0.15	1.27 ± 0.10	2.21 ± 0.15	2.37 ± 0.15
0.75	2.41 ± 0.70	1.94 ± 0.23	2.33 ± 0.18	2.17 ± 0.16	1.83 ± 0.14	2.00 ± 0.22	1.28 ± 0.11	2.10 ± 0.14	2.53 ± 0.20
0.85	1.73 ± 0.76	2.02 ± 0.39	3.02 ± 0.45	3.00 ± 0.28	1.81 ± 0.24	2.09 ± 0.39	1.32 ± 0.17	2.22 ± 0.19	2.58 ± 0.28
0.95	—	—	3.91 ± 1.25	4.32 ± 0.56	1.97 ± 0.59	2.41 ± 1.14	0.99 ± 0.17	2.30 ± 0.25	2.95 ± 0.44

Table 8. Cross-sections in $\mu\text{b}/\text{sr}$ for the reaction $pp \rightarrow pK^+\Lambda$, $p_{beam} = 3200 \text{ MeV}/c$, $\epsilon = 284 \text{ MeV}$, fig. 8.

$\cos \theta$	$\frac{d\sigma}{d\Omega}(\theta_p^*)$	$\frac{d\sigma}{d\Omega}(\theta_{K^+}^*)$	$\frac{d\sigma}{d\Omega}(\theta_\Lambda^*)$	$\frac{d\sigma}{d\Omega}(\theta_{bp}^{Rp\Lambda})$	$\frac{d\sigma}{d\Omega}(\theta_{bK}^{RKp})$	$\frac{d\sigma}{d\Omega}(\theta_{bK}^{RKA})$	$\frac{d\sigma}{d\Omega}(\theta_{Kp}^{Rp\Lambda})$	$\frac{d\sigma}{d\Omega}(\theta_{\Lambda K}^{RKp})$	$\frac{d\sigma}{d\Omega}(\theta_{p\Lambda}^{RKA})$
-0.90	4.41 ± 0.52	2.45 ± 1.31	—	5.07 ± 0.70	2.98 ± 0.76	4.44 ± 1.22	3.49 ± 0.38	2.63 ± 1.13	2.80 ± 0.83
-0.70	2.92 ± 0.26	2.95 ± 0.71	—	2.89 ± 0.28	2.85 ± 0.45	3.03 ± 0.51	3.37 ± 0.32	2.34 ± 0.49	1.84 ± 0.34
-0.50	2.11 ± 0.21	2.96 ± 0.36	—	2.12 ± 0.19	2.65 ± 0.30	2.42 ± 0.26	2.92 ± 0.26	1.92 ± 0.30	2.62 ± 0.29
-0.30	1.98 ± 0.25	2.58 ± 0.26	—	1.90 ± 0.17	2.18 ± 0.18	2.18 ± 0.20	2.77 ± 0.29	2.31 ± 0.26	1.72 ± 0.20
-0.10	2.59 ± 0.40	2.92 ± 0.29	—	1.60 ± 0.17	2.77 ± 0.21	2.46 ± 0.20	2.58 ± 0.24	1.99 ± 0.22	2.09 ± 0.20
0.10	1.83 ± 0.42	2.76 ± 0.29	1.45 ± 0.35	1.71 ± 0.17	2.46 ± 0.20	1.98 ± 0.18	2.15 ± 0.22	2.65 ± 0.27	2.26 ± 0.24
0.30	1.97 ± 0.66	2.78 ± 0.32	1.74 ± 0.19	1.72 ± 0.16	2.89 ± 0.24	2.17 ± 0.19	2.26 ± 0.27	2.85 ± 0.26	2.99 ± 0.29
0.50	2.16 ± 0.99	2.43 ± 0.32	2.15 ± 0.20	1.82 ± 0.17	2.78 ± 0.26	2.45 ± 0.28	2.01 ± 0.26	2.57 ± 0.23	2.82 ± 0.32
0.70	—	2.10 ± 0.38	3.12 ± 0.36	2.62 ± 0.28	3.06 ± 0.38	2.33 ± 0.45	1.08 ± 0.23	3.19 ± 0.30	2.62 ± 0.37
0.90	—	—	4.77 ± 0.95	4.93 ± 0.74	2.54 ± 0.47	3.46 ± 1.27	1.10 ± 0.48	2.79 ± 0.38	3.47 ± 0.79

Table 9. Cross-sections in $\mu\text{b}/\text{sr}$ for the reaction $pp \rightarrow pK^+\Sigma^0$, $p_{beam} = 3059 \text{ MeV}/c$, $\epsilon = 162 \text{ MeV}$, fig. 10.

$\cos \theta$	$\frac{d\sigma}{d\Omega}(\theta_p^*)$	$\frac{d\sigma}{d\Omega}(\theta_{K^+}^*)$	$\frac{d\sigma}{d\Omega}(\theta_{\Sigma^0}^*)$	$\frac{d\sigma}{d\Omega}(\theta_{bp}^{Rp\Sigma^0})$	$\frac{d\sigma}{d\Omega}(\theta_{bK}^{RKp})$	$\frac{d\sigma}{d\Omega}(\theta_{bK}^{RKS})$	$\frac{d\sigma}{d\Omega}(\theta_{Kp}^{Rp\Sigma^0})$	$\frac{d\sigma}{d\Omega}(\theta_{\Sigma^0 K}^{RKp})$	$\frac{d\sigma}{d\Omega}(\theta_{p\Sigma^0}^{RKS})$
-0.90	0.26 ± 0.05	0.34 ± 0.11	—	0.33 ± 0.07	0.33 ± 0.10	0.40 ± 0.12	0.36 ± 0.07	0.35 ± 0.12	0.16 ± 0.05
-0.70	0.31 ± 0.05	0.30 ± 0.06	—	0.27 ± 0.05	0.35 ± 0.07	0.28 ± 0.06	0.32 ± 0.06	0.34 ± 0.07	0.18 ± 0.04
-0.50	0.29 ± 0.05	0.26 ± 0.04	—	0.27 ± 0.04	0.31 ± 0.05	0.27 ± 0.05	0.27 ± 0.05	0.25 ± 0.05	0.26 ± 0.05
-0.30	0.23 ± 0.04	0.26 ± 0.04	—	0.27 ± 0.04	0.22 ± 0.04	0.28 ± 0.04	0.28 ± 0.05	0.27 ± 0.05	0.24 ± 0.04
-0.10	0.23 ± 0.04	0.23 ± 0.04	—	0.25 ± 0.04	0.21 ± 0.03	0.25 ± 0.04	0.28 ± 0.05	0.29 ± 0.05	0.28 ± 0.05
0.10	0.23 ± 0.05	0.18 ± 0.03	0.30 ± 0.05	0.26 ± 0.04	0.20 ± 0.03	0.27 ± 0.04	0.25 ± 0.04	0.29 ± 0.05	0.29 ± 0.05
0.30	0.29 ± 0.07	0.26 ± 0.05	0.28 ± 0.05	0.26 ± 0.04	0.21 ± 0.03	0.27 ± 0.04	0.25 ± 0.04	0.25 ± 0.04	0.30 ± 0.05
0.50	0.27 ± 0.09	0.31 ± 0.06	0.28 ± 0.05	0.30 ± 0.05	0.26 ± 0.04	0.27 ± 0.04	0.28 ± 0.05	0.29 ± 0.05	0.31 ± 0.06
0.70	0.40 ± 0.20	0.32 ± 0.08	0.28 ± 0.05	0.30 ± 0.06	0.32 ± 0.07	0.27 ± 0.06	0.21 ± 0.05	0.23 ± 0.04	0.25 ± 0.05
0.90	—	0.35 ± 0.17	0.34 ± 0.10	0.25 ± 0.06	0.34 ± 0.12	0.33 ± 0.12	0.19 ± 0.06	0.32 ± 0.06	0.36 ± 0.08

Open Access This article is distributed under the terms of the Creative Commons Attribution Noncommercial License which permits any noncommercial use, distribution, and reproduction in any medium, provided the original author(s) and source are credited.

References

1. D. Grzonka, K. Kilian, Nucl. Phys. A **626**, 41C (1997).
2. J.T. Balewski *et al.*, Nucl. Phys. A **626**, 85C (1997).
3. J.T. Balewski *et al.*, Phys. Lett. B **420**, 211 (1998).
4. S. Severin *et al.*, Phys. Rev. Lett. **83**, 682 (1999).
5. P. Kowina *et al.*, Eur. Phys. J. A **22**, 293 (2004).
6. M. Abd El-Samad *et al.*, Phys. Lett. B **632**, 27 (2006).
7. Yu. Valdau *et al.*, Phys. Lett. B **652**, 245 (2007) (e-print: nucl-ex/0703044).
8. A. Baldini *et al.*, *Landolt-Börnstein: Numerical Data and Functional Relationships in Science and Technology, New Series*, Vol. **I/12b** (Springer, New York, Heidelberg, 1988).
9. J.J. De Swart, Rev. Mod. Phys. **35**, 916 (1963).
10. A.A. Sibirtsev *et al.*, Eur. Phys. J. A **29**, 363 (2006).
11. R. Shyam, Phys. Rev. C **73**, 035211 (2006) (nucl-th/0512007).
12. B.C. Lui, B.S. Zou, Phys. Rev. Lett. **96**, 042002 (2006).
13. A. Gasparian *et al.*, Phys. Lett. B **480**, 273 (2000).
14. M. Dillig, M. Schott, arXiv: nucl-th/0604059v1.
15. R. Frascaria *et al.*, Nuovo Cimento A **102**, 561 (1989).
16. R. Siebert, Nucl. Phys. A **567**, 819 (1994).
17. J.-M. Laget, Phys. Lett. B **259**, 24 (1991).
18. J.-M. Laget, Nucl. Phys. A **691**, 11c (2001).
19. S. Capstick, W. Roberts, Phys. Rev. D **58**, 074011 (1998).
20. R. Bradford *et al.*, Phys. Rev. C **73**, 035202 (2006).
21. M. Sumihama *et al.*, Phys. Rev. C **73**, 035214 (2006).
22. K. Hicks *et al.*, Phys. Rev. C **76**, 042201(R) (2007).
23. T. Mart, A. Sulaksono, Phys. Rev. C **74**, 055203 (2006).
24. M.Q. Tran *et al.*, Phys. Lett. B **445**, 20 (1998).
25. PDG06 (W.-M. Yao *et al.*), J. Phys. G **33**, 1 (2006).
26. A.V. Sarantsev *et al.*, Eur. Phys. J. A **25**, 441 (2005).
27. J.W.C. McNabb *et al.*, Phys. Rev. C **69**, 042201(R) (2004).
28. K.-H. Glander *et al.*, Eur. Phys. J. A **19**, 251 (2004).
29. G. Penner, U. Mosel, Phys. Rev. C **66**, 055212 (2002).
30. S. Capstick, C. Roberts, Prog. Part. Nucl. Phys. **45**, 2541 (2000).
31. W. Eyrich, Eur. Phys. J. A **31**, 435 (2007).
32. W. Schroeder for the COSY-TOF Collaboration, Eur. Phys. J. A **31**, 503 (2007).
33. M. Abdel-Bary *et al.*, Phys. Lett. B **649**, 252 (2007).
34. M. Dahmen, PhD Thesis, Rheinische Friedrich-Wilhelms-Universität Bonn, Jülich-3140, ISSN 0944-2952 (1995).

35. R. Bilger *et al.*, Phys. Lett. B **420**, 217 (1998).
36. A. Hassan *et al.*, Nucl. Instrum. Methods Phys. Res. A **425**, 403 (1999).
37. M. Dahmen *et al.*, Nucl. Instrum. Methods Phys. Res. A **348**, 97 (1994).
38. A. Böhm *et al.*, Nucl. Instrum. Methods Phys. Res. A **443**, 238 (2000).
39. M. Schulte-Wissermann, PhD Thesis, TU Dresden (2004).
40. M. Abdel-Bary *et al.*, Phys. Lett. B **662**, 14 (2008).
41. M. Abdel-Bary *et al.*, Phys. Lett. B **647**, 351 (2007).
42. M. Abdel-Bary *et al.*, Eur. Phys. J. A **44**, 7 (2010).
43. S. Brand, PhD Thesis, Ruhr-Universität Bochum (1995).
44. U. Zielinsky, PhD Thesis, Ruhr-Universität Bochum (1999).
45. D. Albers *et al.*, Phys. Rev. Lett. **78**, 1652 (1997).
46. J. Dietrich, Diploma Thesis, TU Dresden, 2006.
47. W.J. Fickinger *et al.*, Phys. Rev. **125**, 2082 (1962).
48. G. Fälldt, C. Wilkin, Z. Phys. A **357**, 241 (1997).
49. M. Abdel-Bary *et al.*, Phys. Lett. B **688**, 142 (2010).
50. E. Byckling, K. Kajantie, *Particle Kinematics* (John Wiley & Sons, 1973).
51. K. Gottfried, J.D. Jackson, Nuovo Cimento **33**, 309 (1964).
52. T.M. Knasel *et al.*, Phys. Rev. D **11**, 1 (1975).
53. R.D. Baker *et al.*, Nucl. Phys. B **141**, 29 (1978).
54. F. Balestra *et al.*, Phys. Rev. Lett. **83**, 1534 (1999).
55. I.M. Blatt, L.C. Biedenharn, Rev. Mod. Phys. **24**, 258 (1952).
56. A. A. Sibirtsev *et al.*, Eur. Phys. J. A **27**, 269 (2006).
57. T. Yamazaki *et al.*, Phys. Rev. Lett. **104**, 13250 (2010).